Pattern formation in Cahn-Hilliard models for Langmuir-Blodgett transfer

Strukturbildung in Cahn-Hilliard-Modellen für Langmuir-Blodgett-Transfer

als Masterarbeit vorgelegt von
Markus Wilczek

Dezember 2012

Westfälische Wilhelms-Universität Münster

Contents

1 Introduction

Coating objects with thin films of a certain material is ubiquitous nowadays, covering a wide range of applications like lens coatings that improve reflection properties [MKS+12] or coatings that enhance the rigidity and durability [RL07]. The definition of *thin* in *thin films* is hard to give as the term is used for films with a thickness of a few microns as well as for films with just a few nanometers. While the upper boundary for the thickness of thin films is quite fuzzy, the lower boundary can be defined precisely because the minimal thickness of a film is determined by the size of a single molecule of its constituents. In literature, the term thin film is mostly used for films, where the thickness is small compared to the length scale at which lateral variations occur [ODB97]. If the thickness of a film corresponds to one molecular layer, it is referred to as a *monolayer*. The actual thickness of monolayers varies greatly with the actual material, ranging from just a few ångström up to a few tens of nanometers [GK97].

A common method to produce and transfer monolayers is the so-called Langmuir-Blodgett transfer [Rob90]. The name refers to Irving Langmuir (1881–1957), an American chemist and physicist, and his coworker at *General Electric*, Katherine Burr Blodgett (1898–1979), also a physicist. Their work based upon techniques developed by Agnes Pockels (1862–1935) who did experiments on surfaces of liquids [Poc91]. Among others, she studied the influence of solutes and surface acting agents (also referred to as surfactants) on the surface tension of water with a self-designed apparatus, today called Pockels trough [Poc93]. Langmuir and Blodgett developed it further to the so-called Langmuir-Blodgett trough which can be used to prepare and transfer monolayers [Blo34, Lan34, Blo35].

The first step in Langmuir-Blodgett transfer is the preparation of a monolayer of the molecules to be transferred on a liquid bath. This can be easily achieved for amphiphilic substances like, e.g., the pulmonary surfactant dipalmitoylphosphatidylcholine (DPPC), of which the chemical structure is shown in Fig. 1.1.

Such substances consist of molecules that have hydrophilic as well as hydrophobic (or lipophilic) parts. In the case of DPPC the molecules have one polar hydrophilic *head* and a hydrophobic *tail* consisting of long nonpolar hydrocarbon chains. When brought into contact with a water surface, the molecules try to arrange themselves in a way that their hydrophobic tails point away from the water surface in order to minimize their energetic state. This automatically leads to the formation of a monolayer of the surfactant on the water surface. In this case, the surfactant is confined to the water surface and therefore constitutes a truly two-dimensional system. Depending on exterior parameters, the monolayer can be in different states that especially vary in their density and the way the nonpolar tails of the molecules are arranged. Besides a gaseous state,

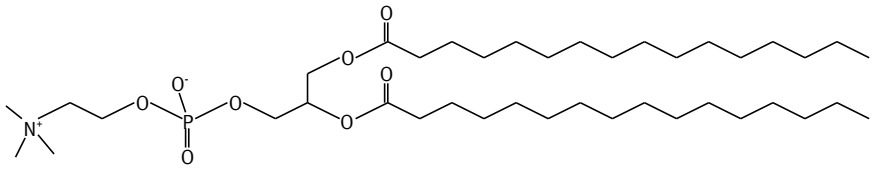

Figure 1.1: Chemical structure of the pulmonary surfactant dipalmitoylphosphatidylcholine (DPPC). The molecules posses a polar, hydrophilic *head* (left side) and a nonpolar, hydrophobic *tail* (right side).

different liquid states exist that vary in the mean distance between the molecules and whether the nonpolar tails of the molecules are aligned. This is only true for the liquid-condensed (LC) phase, in contrast to the liquid-expanded (LE) phase. Both states are illustrated in Fig. 1.2. In a Langmuir-Blodgett trough, movable barriers can be used to control the area of the water surface that is accessible for the surfactant film. In this way, also the phase of the film can be controlled.

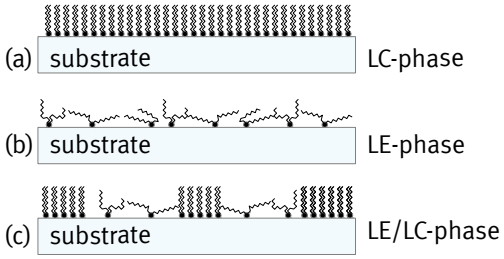

Figure 1.2: Illustration of the phases occurring in Langmuir-Blodgett transfer: (a) liquid-expanded (LE) and (b) liquid-condensed (LC), as well as (c) alternating domains in the LE and LC phase.

After the monolayer is prepared, it can be transferred to a substrate by simply drawing the substrate out of the trough. A sketch of a Langmuir-Blodgett trough and the transfer process is depicted in Fig. 1.3. During the transfer, the barriers need to be permanently adjusted to ensure a constant density of the monolayer. Remarkably, the monolayer is not necessarily transferred as it has been prepared on the liquid surface, but can also undergo a phase transition, for example from a LE phase on the water surface to a LC phase on the substrate. This happens due to an effect called *substrate-mediated condensation* (SMC). This effect describes a short-range interaction between the monolayer and the substrate that is negligible for thick water layers, but has significant influence on the thermodynamics of the monolayer as the water layer vanishes during the transfer process [RS92]. The SMC reduces the value of the free energy of the LC phase and therefore favors the condensation of the monolayer. It is a remarkable fact that this condensation does not necessarily occur uniformly in space and

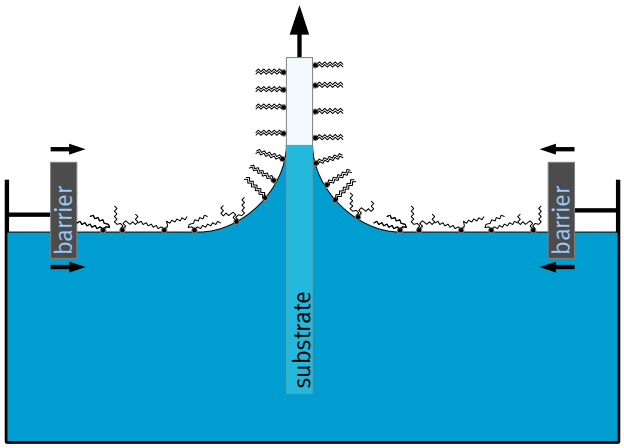

Figure 1.3: Illustration of a Langmuir-Blodgett trough used for Langmuir-Blodgett transfer. The movable barriers can be used to control the density as well as the phase of the surfactant film.

time, but may lead to the transfer of complex patterns of different phases. Figure 1.4 shows images made with atomic force microscopy that exhibit the patterns arising during Langmuir-Blodgett transfer of DPPC. Depending on the transfer velocity, the stripes are parallel or perpendicular to the pull-direction (depicted by the white arrows in Fig. 1.4). The width of the stripes is of a few hundred nanometers and is uniform over macroscopic areas of several cm^2 [CLH$^+$07]. Hence, by one simple transfer process one is able to produce patterns with hundreds of thousands of perfectly aligned stripes.

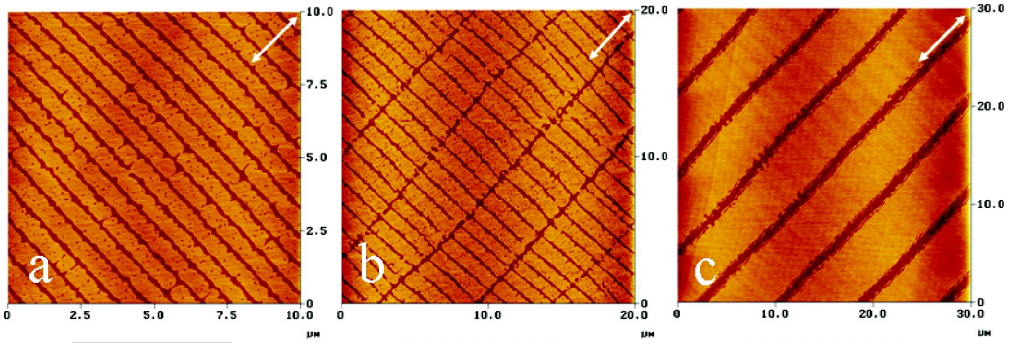

Figure 1.4: AFM images of occurring patterns of DPPC in the liquid-condensed and liquid-expanded phase after Langmuir-Blodgett transfer at different transfer velocities: a) 60 mm/min, b) 40 mm/min, c) 10 mm/min. The white arrows depict the transfer direction, the scale of the axes are microns. Taken from [CLH$^+$07].

Recently, Köpf et al. have developed a model which is able to reproduce the experimental findings of pattern formation phenomena in Langmuir-Blodgett

transfer and can be used to investigate this process from a theoretical point of view [KGF09, KGFC10, Köp11]. The model couples the dynamics of a thin fluid layer with the thermodynamics of the monolayer in the vicinity of the LE/LC phase transition.

The dynamics of the thin fluid layer can be approximately described by the Navier-Stokes equation in the so-called lubrication approximation [ODB97]. This approximation holds true for fluid layers with a thickness that is small compared to the characteristic wave length of variations in lateral direction, which is the case for the water layer in the vicinity of the air-water-substrate contact line.

The thermodynamics of the monolayer is modeled with a Cahn-Hilliard type free energy in the vicinity of a phase transition. The coupling between the monolayer and the water layer mainly occurs due to two effects. On the one hand, the monolayer influences the surface tension of the fluid layer, depending on the local concentration of the monolayer. On the other hand, as mentioned above, the monolayer is subject to substrate-mediated condensation that is strongly dependent on the distance between the substrate and the monolayer, and therefore strongly dependent on the height profile of the water layer. We will skip the precise derivation of the model and refer the interested reader to [Köp11]. Taking all the aforementioned effects into account, the evolution equations for the height of the water layer $H(\mathbf{x}, T)$ and the density of the monolayer $\Gamma(\mathbf{x}, T)$ have been obtained,

$$\begin{aligned}\frac{\partial}{\partial T} H = -\nabla \cdot \Bigg[& \frac{H^3}{3} \underbrace{\nabla \left\{ \left(1 - \epsilon^2 P_{\text{hom}}\right) \Delta H - \Pi \right\}}_{\text{generalized pressure gradient}} \\ & + \underbrace{\frac{H^2}{2} \left(\epsilon^{-2} \Gamma \nabla \Delta \Gamma - \nabla P_{\text{hom}} \right)}_{\text{Marangoni forces}} - \underbrace{H \mathbf{V}}_{\text{advection}} \Bigg] + \underbrace{Q}_{\text{sink}}, \end{aligned} \tag{1.1}$$

$$\begin{aligned}\frac{\partial}{\partial T} \Gamma = -\nabla \cdot \Bigg[& \frac{\Gamma H^2}{2} \underbrace{\nabla \left\{ \left(1 - \epsilon^2 P_{\text{hom}}\right) \Delta H - \Pi \right\}}_{\text{generalized pressure gradient}} \\ & + \underbrace{\Gamma H \left(\epsilon^{-2} \Gamma \nabla \Delta \Gamma - \nabla P_{\text{hom}} \right)}_{\text{Marangoni forces}} - \underbrace{\Gamma \mathbf{V}}_{\text{advection}} + \underbrace{\mathbf{I}}_{\text{diff. flux}} \Bigg]. \end{aligned} \tag{1.2}$$

Here, the spatial vector $\mathbf{x} = (X, Y)$ is in general two-dimensional. The first component X is chosen to be in the direction of the pull process.

Both equations include contributions from a generalized pressure gradient, Marangoni forces occurring due to surface tension gradients, advection terms accounting for the pulling during the transfer process, and source or sink terms incorporating evaporation as well as diffusive flux of the surfactant layer. The generalized pressure comprises contributions arising in the case of homogeneous

liquid layers without any surfactants. P_{hom} denotes this pressure apparent in a homogeneous situation and ϵ is a parameter of smallness originating from the lubrication approximation. Besides the Laplace pressure term $\propto \Delta H$, the generalized pressure comprises the so-called disjoining pressure $\Pi(H)$, that includes the substrate-mediated condensation. The specific shape of $\Pi(H)$ is not known in general up to date. Usually, combinations of short range and long range interactions with different signs are used in this context, e.g., Lennard-Jones potentials [ODB97].

The ability of surfactants to change the surface tension of the underlying liquid introduces the possibility for the surface tension to be spatially varying with the concentration of the surfactant. Such a spatially inhomogeneous surface tension leads to forces called *Marangoni forces* that create an important coupling between the thermodynamics of the surfactant layer and the dynamics of the fluid.

In order to model the transfer process with Eqs. (1.1)-(1.2), two choices of a coordinate system are conceivable: a coordinate system that is at rest in relation to the substrate being pulled out the trough, or one that is at rest in relation to the trough and laboratory system. This choice determines what boundary conditions must be applied at the boundary of the simulation domain and whether an advection term has to be added to the equations. For Eqs. (1.1)-(1.2), the coordinate system is chosen to be at rest in relation to the trough, which necessitates the presence of the advection terms with the transfer velocity $\mathbf{V}$ in both equations. In addition, the presence of the trough ensures a constant height H_0 of the water layer and a constant surfactant density Γ_0 at the lower boundary ($X = 0$) of the simulation domain. At the upper boundary ($X = L$), non-reflective boundary conditions would be an ideal choice but are hard to implement for such equations. Easier to implement and also well-suited for this application are vanishing first- and second-order derivatives with respect to X of both fields $H(X,T)$ and $\Gamma(X,T)$ at the upper boundary, that have proven to be nearly non-reflective. Thus, the boundary conditions read

$$\Gamma|_{X=0} = \Gamma_0, \quad \left.\frac{\partial^2 \Gamma}{\partial X^2}\right|_{X=0} = 0, \quad \left.\frac{\partial \Gamma}{\partial X}\right|_{X=L} = 0, \quad \left.\frac{\partial^2 \Gamma}{\partial X^2}\right|_{X=L} = 0, \tag{1.3}$$

$$H|_{X=0} = H_0, \quad \left.\frac{\partial^2 H}{\partial X^2}\right|_{X=0} = 0, \quad \left.\frac{\partial H}{\partial X}\right|_{X=L} = 0, \quad \left.\frac{\partial^2 H}{\partial X^2}\right|_{X=L} = 0. \tag{1.4}$$

For two-dimensional simulations, periodic boundary conditions are applied for the Y-direction.

This model has been successful in reproducing experimental findings of pattern formation phenomena in Langmuir Blodgett transfer [KGFC10] and to predict up to then not investigated behavior like synchronization with prestructured substrates [KGF11]. However, this two-component model is quite complicated. Additionally, Köpf et al. [Köp11] noticed that temporal changes of the height profile $H(X,T)$ of the water nearly vanished and therefore the meniscus remained almost static during the transfer process. As further evidence to this fact, the meniscus can be manually frozen during the simulations, without influencing the transfer and patterning process significantly [Köp11].

This led to the assumption that a more simplified model should also be able to reproduce the experimental findings, while allowing for extended mathematical treatments to investigate it in more detail due to a less complex mathematical structure [KGFT12].

The first step toward a simplified model is to use the fact that the meniscus shape remains almost static and therefore to set $\frac{\partial H}{\partial T} = 0$. Hence, the first Eq. (1.1) shows no more dynamics and only defines the shape of the static meniscus, which will enter the second Eq. (1.2) merely parametrically. A further investigation of Eq. (1.2) reveals that a static meniscus minimizes the contributions of the generalized pressure gradient. This means that this term can be approximately neglected in comparison to the other contributions. Therefore, one is then left with the equation

$$\frac{\partial}{\partial T}\Gamma = -\nabla \cdot \left[\underbrace{\Gamma H \left(\epsilon^{-2} \Gamma \nabla \Delta \Gamma - \nabla P_{\mathrm{hom}} \right)}_{\text{Marangoni forces}} - \underbrace{\Gamma \mathbf{V}}_{\text{advection}} + \underbrace{\mathbf{I}}_{\text{diff. flux}} \right]. \tag{1.5}$$

Omitting the diffusive flux $\mathbf{I}$ because of its minor influence [Köp11], Eq. (1.5) can be rewritten to

$$\frac{\partial}{\partial T}\Gamma = -\nabla \cdot \left[-\Gamma H \epsilon^{-2} \nabla \left(\Gamma \Delta \Gamma - \frac{1}{2} \left(\nabla \Gamma \right)^2 + \epsilon^2 P_{\mathrm{hom}} \right) \right] + \mathbf{V} \cdot \nabla \Gamma. \tag{1.6}$$

Equation (1.6) possesses the form of a generalized Cahn-Hilliard equation that will be discussed in the next chapter. This reduced model has proven to still be able to reproduce experimental findings as well as to be more easy to treat from a mathematical point of view [Köp11, KGFT12]. Therefore, we investigate this reduced Cahn-Hilliard model in detail during this thesis.

This thesis is organized as follows:

Chapter 2 contains a derivation of the Cahn-Hilliard model that is used to model pattern formation phenomena during Langmuir-Blodgett transfer. The main concepts of spinodal decomposition, which are the basis for Cahn-Hilliard models, are discussed here, as well as all the effects that are incorporated in our model, like the ansatz for the free energy of the monolayer in the vicinity of the LE/LC phase transition, energetic boundary layer contributions, and SMC. Because even the reduced Cahn-Hilliard model cannot be solved analytically, numerical treatments of the underlying equations have to be used. The techniques needed, including Runge-Kutta time stepping methods, finite difference methods and the implementation on modern graphics processors, are presented in chapter 3. In chapter 4, the model is applied to the case of transfer onto homogeneous substrates. Properties of the occurring patterns in one and two dimensions are discussed in dependence of experimental parameters like the transfer velocity. In addition, a novel approach to produce gradient structures, Langmuir-Blodgett rotating transfer, is examined with simulations. Besides homogeneous substrates, also the transfer onto substrates that have some kind of prestructure is discussed in chapter 5. As it is shown there, prestructures can be used to control the patterning process during the transfer via the occurrence of synchronization phenomena. Chapter 6 provides a linear stability analysis

for solutions of the model. They are used to gain more insights in the origin of the patterning process. In addition, the emergence of stripe patterns of different orientations in two-dimensional systems is investigated. The last chapter 7 contains a summary of the whole thesis and raises some possible questions for future research.

2 Model

Cahn-Hilliard models are in general able to describe binary mixtures in the framework of spinodal decomposition. Therefore, a short introduction to spinodal decomposition will be given here, followed by a derivation of the model equations for Langmuir-Blodgett transfer that will be employed in the following.

2.1 Spinodal decomposition

The term spinodal decomposition occurs in the context of phase transitions. A rather simple yet insight-generating system that can be utilized to explain the basic concepts is the van der Waals equation. It is an extension to the ideal gas equation with additional contributions to the pressure due to interactions between the gas molecules as well as contributions to the available volume due to the volume occupied by the gas molecules. The van der Waals equation reads [Dem03]

$$\left(p + a\frac{n^2}{V^2}\right)(V - nb) = nRT. \tag{2.1}$$

Here, p denotes the pressure of a gas with n moles of molecules in a confined volume V at a certain temperature T. R is the gas constant and a and b are gas specific constants depending on the attraction between the molecules and the volume excluded by them. A lot of gases are described well with this model, for example carbon dioxide (CO_2), with the values $a = 3.65 \cdot 10^6 \, \frac{\text{bar}\cdot\text{cm}^6}{\text{mol}^2}$ and $b = 42.5 \, \frac{\text{cm}^3}{\text{mol}}$ [Dem03]. For a given temperature, Eq. (2.1) specifies a line in a pressure vs. volume diagram, which is called an isotherm. Figure 2.1 shows such a diagram with four isotherms for different temperatures. For temperatures below a certain critical temperature T_{crit}, the isotherms have a local minimum and a local maximum, which necessitates a region where

$$\frac{\partial p}{\partial V} > 0. \tag{2.2}$$

This is physically impossible, as this means an infinitesimal decrease $dV < 0$ of the volume would lead to a decrease $dp < 0$ of the pressure, resulting in an unphysical behavior of the system. This stems from the assumption of a homogeneous phase in the derivation of the van der Waals equation, that does not hold true below T_{crit}. Therefore, a phase transition has to occur in the region of positive $\frac{\partial p}{\partial V}$. In this region, which is separated from the rest of the phase diagram by the so-called *spinodal*, both phases coexist with a volume share that can be calculated from the overall free energy of the system. This process leading to the separation of phases is called *spinodal decomposition*.

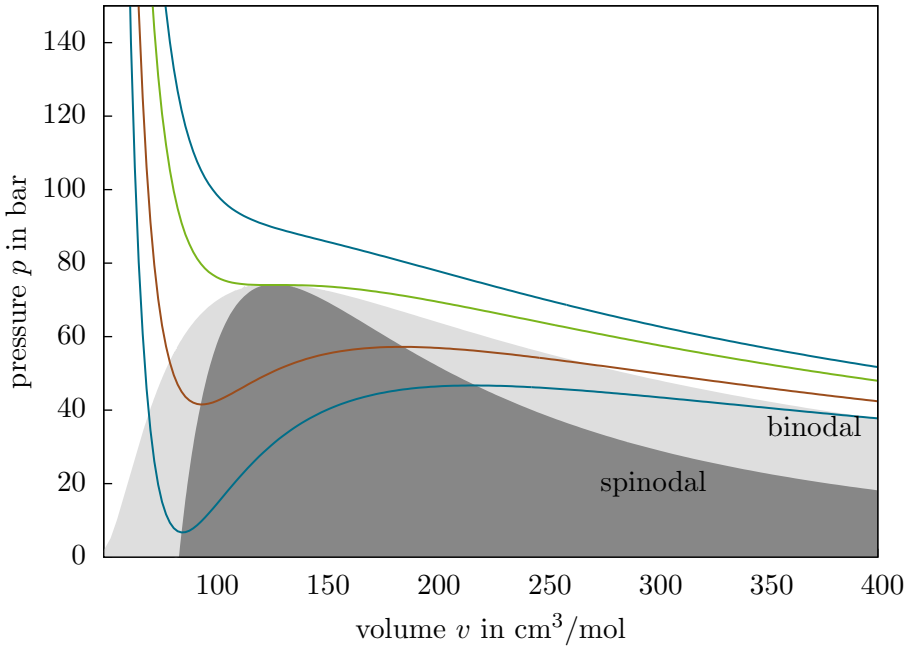

Figure 2.1: Isotherms of carbon dioxide in a van der Waals gas model. From top to bottom: $T = 320\,\mathrm{K}$ (blue line), $T = T_{\mathrm{crit}} \approx 304\,\mathrm{K}$ (green line), $T = 280\,\mathrm{K}$ (red line), $T = 260\,\mathrm{K}$ (blue line). The light gray area depicts the binodal region and the dark gray area depicts the spinodal region.

However, it can be energetically advantageous for the system to separate into different phases even outside the spinodal. This area can be found by the famous Maxwell construction [Nol12], which continuously replaces a part of the isotherm with a line of constant pressure p_{m}. This pressure is chosen in a way that

$$\int_{V_{\mathrm{a}}}^{V_{\mathrm{b}}} p(V)dV = \int_{V_{\mathrm{a}}}^{V_{\mathrm{b}}} p_{\mathrm{m}}dV = p_{\mathrm{m}}(V_{\mathrm{b}} - V_{\mathrm{a}}), \tag{2.3}$$

where V_{a} and V_{b} denote the left and right boundary between which the isotherm is replaced by the line of constant pressure p_{m}. This implies that the energy needed to drive the system through the phase transition is not affected by the Maxwell construction. The region where the Maxwell construction is possible is separated from the rest of the p-V-plane by the so-called *binodal*. Inside the binodal, but outside the spinodal, the system may, but does not have to undergo a partial phase transition. Superheated fluids or subcooled gases are experimentally realizable examples for systems inside the binodal, that are in a homogeneous state, although their total energy would decrease if they were not.

Binodal and spinodal of course meet, as soon as the minimum and maximum of $p(V)$ merge at $T = T_{\mathrm{crit}}$ in the so called *critical point*. Above this critical point, no different phases can be distinguished.

Although this discussion treated a rather simple example, the basic principles

of phase transitions, binodals, spinodals etc. remain the same even for more complex systems, as they will be considered in the following.

2.2 The Cahn-Hilliard equation

While the considerations above dealt with the question in what kind of state (homogeneous or phase separated) a system is, we now want to describe the system more detailed and especially want to investigate the process of spinodal decomposition. This can be done with the Cahn-Hilliard equation. The derivation given here follows along the lines of [NCS84], to which we refer the reader for more details.

We consider a binary mixture of the two components A and B. The local density of the components is called $c_\mathrm{A}(\mathbf{x},t)$ and $c_\mathrm{B}(\mathbf{x},t)$, where $\mathbf{x}$ is a two dimensional vector comprising $\mathbf{x}=(x,y)$. Each component has a corresponding flux $\mathbf{J}_\mathrm{A}(\mathbf{x},t)$ and $\mathbf{J}_\mathrm{B}(\mathbf{x},t)$. The flux can in general be expressed as a function of the mobility M_ij from component i to component j and the gradients of the chemical potentials μ_i of each component, with $\mathrm{i}=\mathrm{A},\mathrm{B}$,

$$\mathbf{J}_\mathrm{A} = -M_\mathrm{AA}\nabla\mu_\mathrm{A} - M_\mathrm{AB}\nabla\mu_\mathrm{B}, \tag{2.4}$$
$$\mathbf{J}_\mathrm{B} = -M_\mathrm{BA}\nabla\mu_\mathrm{A} - M_\mathrm{BB}\nabla\mu_\mathrm{B}. \tag{2.5}$$

Usually we are not interested in the absolute values of the densities and fluxes of each component, but only in the relative ratio between them. Therefore, we can rescale the sum of both densities to one and introduce a net flux. This leaves us with only one density and one flux, namely

$$c(\mathbf{x},t) = c_\mathrm{B}(\mathbf{x},t) = 1 - c_\mathrm{A}(\mathbf{x},t) \quad \text{and} \quad \mathbf{J} = \mathbf{J}_\mathrm{B} - \mathbf{J}_\mathrm{A}. \tag{2.6}$$

Inserting (2.4) and (2.5) into (2.6), one obtains

$$\mathbf{J} = -M_\mathrm{BA}\nabla\mu_\mathrm{A} - M_\mathrm{BB}\nabla\mu_\mathrm{B} + M_\mathrm{AA}\nabla\mu_\mathrm{A} + M_\mathrm{AB}\nabla\mu_\mathrm{B}, \tag{2.7}$$

which can be written more shortly using the Gibbs-Duhem relationship [Nol12]

$$(1-c)\nabla\mu_\mathrm{A} = -c\nabla\mu_\mathrm{B}. \tag{2.8}$$

The expression for the flux then reads

$$\mathbf{J} = -M\nabla(\mu_\mathrm{B} - \mu_\mathrm{A}), \quad \text{with} \tag{2.9}$$
$$M = (1-c)(M_\mathrm{BB} - M_\mathrm{AB}) + c(M_\mathrm{AA} - M_\mathrm{BA}). \tag{2.10}$$

Now M denotes an effective mobility, that is in general dependent on the ratio between the two components. According to classical thermodynamics, the difference between two chemical potentials can be expressed by means of a corresponding free energy per unit volume $f(c)$,

$$\mu_\mathrm{B} - \mu_\mathrm{A} = \frac{\partial f(c)}{\partial c}. \tag{2.11}$$

The Cahn Hilliard equation now follows directly from the assumption of mass conservation:

$$\frac{\partial}{\partial t}c(\mathbf{x},t) = -\nabla\cdot\mathbf{J} = \nabla\cdot\left(M\nabla\frac{\partial f(c)}{\partial c}\right). \tag{2.12}$$

The main task remaining now is to find an appropriate expression for the free energy $f(c)$ that fits the experimental setting.

As the monolayer we want to model with this equation is prepared to be in the vicinity of a phase transition, it seems reasonable to assume a double well potential for the free energy. Probably the easiest expression for this is a quartic polynomial with zero contributions from odd exponents of c, so the potential is symmetric,

$$f(c) = a_4c^4 + a_2c^2. \tag{2.13}$$

The coefficients a_2 and a_4 can be chosen according to the desired positions of the local minima of the free energy, for example $a_4 = 1/4$ and $a_2 = -1/2$, which means that $c = \pm 1$ correspond to states of minimal free energy.

2.2.1 Energetic boundary layer contributions

Up to now, no influence of boundary layers between regions of different c are considered. A more realistic model should contain some kind of penalization for the creation of more regions and boundaries to account for the accompanying increase of entropy. This leads to considerations made first by Cahn and Hilliard [CH58]. They derived an expression for a generalized free energy potential that incorporates boundary contributions, which we want to derive here briefly, too. We start with a generalization of the free energy that allows for taking into account spatial inhomogeneities via an expansion of gradient terms:

$$f(c) \to \hat{f}(c,\nabla c,\nabla^2 c,...) = f(c)+\mathbf{L}\cdot\nabla c+\mathrm{J}\nabla(\nabla c)+\frac{1}{2}\mathrm{K}(\nabla c)(\nabla c)+\text{h.o.t.}, \tag{2.14}$$

where $\mathbf{L}$ is a vector and J and K are matrices containing coefficients for the strength of penalization of boundaries. Because the system we want to describe is isotropic, $\mathbf{L}$, J and K must be isotropic, as well. This reduces $\mathbf{L}$ to zero and J and K to multiples of Kronecker delta, which means there are only three terms contributing up to second order, namely

$$\hat{f}(c,\nabla c,\nabla^2 c,...) = f(c) + J\nabla^2 c + \frac{1}{2}K(\nabla c)^2 + \text{h.o.t.}, \tag{2.15}$$

where J and K are only scalars. It turns out, that also J has to vanish due to arguments based on natural boundary conditions for the boundaries of the whole volume V [NCS84]. This means there is only one contribution up to second order of the ∇-operator, that we can incorporate into the Cahn-Hilliard equation (2.12) via

$$\frac{\partial f(c)}{\partial c} \to \frac{\partial f(c)}{\partial c} - K\Delta c. \tag{2.16}$$

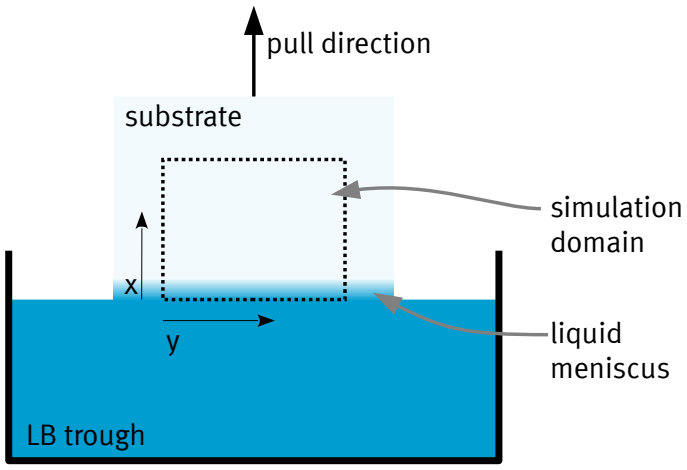

Figure 2.2: Illustration of the position of the frame of reference that is chosen for simulations of the Cahn-Hilliard model. x and y depict the spatial coordinates. Compared to Fig. 1.3, the trough is turned by 90 degrees for this illustration.

2.2.2 Frame of reference

As already mentioned in chapter 1, one has to chose a frame of reference, in which the model should be applied to the experimental setting. Obviously two choices are most reasonable, either the system considered is at rest relative to the Langmuir-Blodgett trough and the laboratory, or the system is at rest relative to the substrate that is pulled out of the trough. Throughout this thesis we will stick with the first type of frame of reference, which is illustrated in Fig. 2.2. This has two implications for the model.

First, as the substrate is pulled out of the trough, it imposes some kind of force on the monolayer, so it gets pulled out too. In the model, this implies that the field $c(\mathbf{x})$ is subject to an advection. In Eq. (2.12) this can be achieved by adding an advective term to the time derivative,

$$\frac{\partial}{\partial t}c(\mathbf{x},t) \rightarrow \frac{\partial}{\partial t}c(\mathbf{x},t) + \mathbf{v}\cdot\nabla c(\mathbf{x},t), \tag{2.17}$$

where $\mathbf{v}$ is a vector specifying the direction and velocity of the pulling.

Second, the spatial region we can simulate with our model is of course limited. That calls for boundary conditions specifying the behavior at the boundaries of the simulation region. At the lower boundary where $\mathbf{x} = (x = 0, y)$ (see Fig. 2.2 for an illustration of the notation of the coordinates), the substrate is in contact with the liquid reservoir of the trough, which continuously supplies molecules of the monolayer with a certain density. The density is kept constant by moving the barriers that were shown in Fig. 1.3. For our model this implies that the value of c is also held constant at the lower boundary. In addition, we

require the second derivative to vanish at the boundary,

$$c|_{x=0} = c_0, \quad \left.\frac{\partial^2}{\partial x^2} c\right|_{x=0} = 0. \tag{2.18}$$

On the upper boundary ($x = L_x$), the boundary should be non-reflective ideally, which means that every flux trough the boundary is not affected by the boundary. Unfortunately, it is hard to formulate such boundary conditions for the kind of equation we are dealing with. We can nevertheless easily formulate boundary conditions, that are effectively non-reflective, which means their influence on the bulk of the simulation domain is limited to a small region around the boundaries. In the simulations it is then possible to choose the simulation domain larger than the region of interest, so that the effects of the boundaries are negligible there. We will use vanishing first and second order derivatives at the upper boundary leading to a smooth behavior at the boundary,

$$\left.\frac{\partial}{\partial x} c\right|_{x=L_x} = 0, \quad \left.\frac{\partial^2}{\partial x^2} c\right|_{x=L_x} = 0. \tag{2.19}$$

Numerical simulations can be used to investigate the influence of the boundary conditions by simply doing the same simulations on different domain sizes. In the case of effectively non-reflective boundary conditions, the deviations of the simulations should be well localized near the boundaries. This holds true for (2.19).

The boundary conditions for the y-direction can be chosen to be periodically, which means that the simulation domain is thought to be repeated in y-direction up to infinity,

$$c(x, y = 0) = c(x, y = L_y). \tag{2.20}$$

2.2.3 Substrate-mediated condensation (SMC)

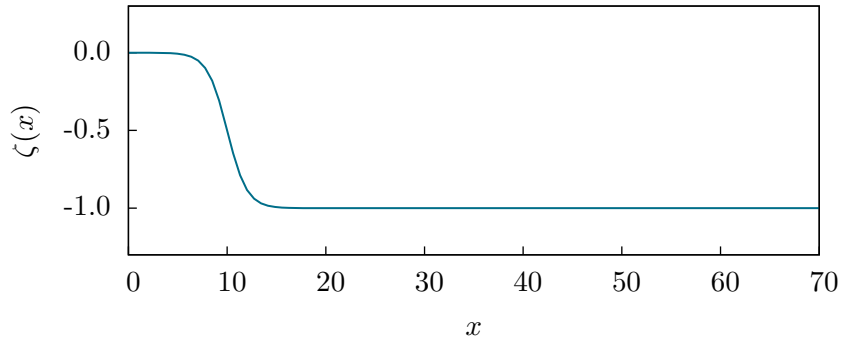

Figure 2.3: Plot of the assumed spatial dependence of the SMC $\zeta(x)$, with $\zeta(x) = -\frac{1}{2}\left(1 + \tanh\left(\frac{x-x_s}{l_s}\right)\right)$, and $x_s = 10$, $l_s = 2$.

Now we want to incorporate the effect of substrate-mediated condensation into our model. As already discussed in chapter 1, SMC is a short range interaction between the substrate and the monolayer favoring the phase transition

of the monolayer into the LC phase. The effect becomes important as the liquid layer separating the substrate and the monolayer vanishes. The SMC therefore has a dependence on the liquid layer height. The height profile could be calculated as the stationary solutions of Eq. (1.1) of the full model. But it turns out that only the qualitative shape of the height profile, that is, a smooth transition from a fixed value at the lower boundary to a lower fixed value after the meniscus, is important for the patterning process. Hence, it can be simply described by a hyperbolic tangent $\zeta(x)$ located at the meniscus. We now interpret the SMC as a skewness of the free energy $f(c)$ favoring the energetic well associated with the LC phase in comparison to the one associated with the LE phase. This can be achieved by adding a term linear in c and proportional to $\zeta(x)$ to the free energy (2.13),

$$f(c,x) = -\frac{1}{2}c^2 + \frac{1}{4}c^4 + \mu\zeta(x)c, \quad \zeta(x) = -\frac{1}{2}\left(1 + \tanh\left(\frac{x - x_\mathrm{s}}{l_\mathrm{s}}\right)\right). \quad (2.21)$$

Here μ is a coefficient that regulates the strength of the SMC, x_s specifies the position of the meniscus and the main step in the strength of the SMC, and l_s determines the steepness of the transition. The function $\zeta(x)$ is designed in a way that it provides a smooth transition from 0 to -1. Unless specified differently, $\mu = 0.5$, $x_\mathrm{s} = 10$ and $l_\mathrm{s} = 2$ are used in this thesis. The graph of $\zeta(x)$ is plotted in Fig. 2.3 and the resulting shape of the free energy $f(c,x)$ is illustrated in Fig. 2.4.

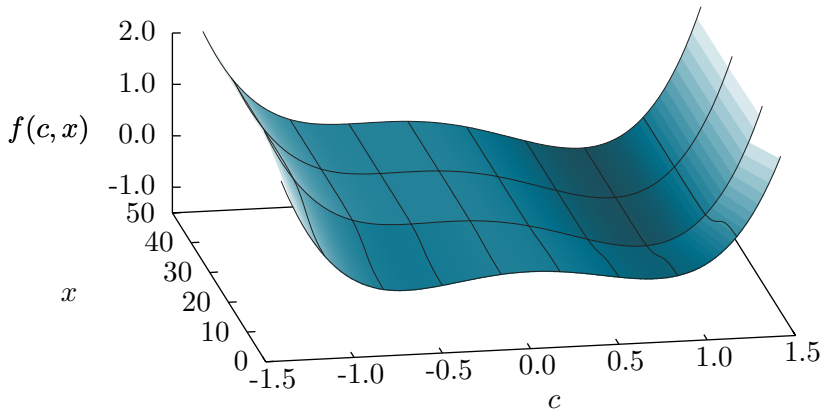

Figure 2.4: Illustration of the free energy landscape $f(c,x) = -\frac{1}{2}c^2 + \frac{1}{4}c^4 + \mu\zeta(x)c$, with $\zeta(x) = -\frac{1}{2}\left(1 + \tanh\left(\frac{x-x_\mathrm{s}}{l_\mathrm{s}}\right)\right)$, $\mu = 0.5$, $x_\mathrm{s} = 10$ and $l_\mathrm{s} = 2$.

2.2.4 The final model

If we now include all of the previous considerations into the Cahn-Hilliard equation, our final model reads

$$\begin{aligned}
\frac{\partial}{\partial t}c(\mathbf{x},t) =& -\nabla\cdot\left[-\nabla\left(-\Delta c - c + c^3 + \mu\zeta(x)\right) + \mathbf{v}c\right], \quad \text{with} \qquad (2.22)\\
\zeta(x) =& -\frac{1}{2}\left(1+\tanh\left(\frac{x-x_\mathrm{s}}{l_\mathrm{s}}\right)\right), \quad \text{and}\\
c|_{x=0} =& c_0, \qquad \frac{\partial^2}{\partial x^2}c\bigg|_{x=0} = 0, \quad \frac{\partial}{\partial x}c\bigg|_{x=L_x} = 0, \quad \frac{\partial^2}{\partial x^2}c\bigg|_{x=L_x} = 0,\\
c|_{y=0} =& \, c|_{y=L_y}\,.
\end{aligned}$$

As it is hardly possible to find exact solutions to this equation analytically, we will discuss how to treat this equation numerically in the following chapter.

3 Numerical Implementation

Equation (2.22) is a partial differential equation in two spatial dimensions that we want to solve numerically as an initial value problem. That means we assume a certain initial configuration $c(\mathbf{x}, t_0)$ and want to determine the evolution of the system in time. As a first step toward a numerical solution of a partial differential equation, the equations have to be discretized onto a spatial and temporal grid. Then the solution can be split into two algorithms, one to evaluate the right-hand side of the equation including the spatial derivatives, and another to integrate in time, the so-called time stepping.

3.1 Runge-Kutta methods

Probably the easiest algorithm for the temporal integration of a differential equation is the so-called explicit Euler method. If we consider the equation

$$\frac{\partial}{\partial t} c(\mathbf{x}, t) = f(c(\mathbf{x}, t), t), \tag{3.1}$$

with a certain initial configuration $c(\mathbf{x}, t_0)$, we can approximate the time derivative by the forward difference quotient

$$\frac{\partial}{\partial t} c(\mathbf{x}, t) \approx \frac{c(\mathbf{x}, t + \Delta t) - c(\mathbf{x}, t)}{\Delta t}, \tag{3.2}$$

with a small, but finite temporal step Δt. With this we can write (3.1) as

$$c(\mathbf{x}, t + \Delta t) = c(\mathbf{x}, t) + \Delta t \cdot f(c(\mathbf{x}, t), t). \tag{3.3}$$

This basically implies that we can evaluate the time evolution of the system by doing small steps given by the right-hand side of the equation. This directly exposes the major drawback of this method: the right-hand side is taken to be constant at the initial value $f(c(\mathbf{x}, t), t)$ for the whole time interval $[t, t + \Delta t]$. Obviously, the step size Δt then has to be sufficiently small for this method to deliver good results.

An improvement over this method are so-called predictor-corrector methods like Heun's method. The idea of this method is to make a preliminary time step with the Euler method,

$$\tilde{c}(\mathbf{x}, t + \Delta t) = c(\mathbf{x}, t) + \Delta t \cdot f(c(\mathbf{x}, t), t), \tag{3.4}$$

and then use this result to approximate the right-hand side at the upper boundary of the time interval $[t, t + \Delta t]$, $f(\tilde{c}(\mathbf{x}, t), t + \Delta t)$. This is now averaged with the value at the lower boundary, $f(c(\mathbf{x}, t), t)$, and used for the real time step

$$c(\mathbf{x}, t + \Delta t) = c(\mathbf{x}, t) + \frac{1}{2} \Delta t \cdot \left(f(c(\mathbf{x}, t), t) + f(\tilde{c}(\mathbf{x}, t + \Delta t), t + \Delta t) \right). \tag{3.5}$$

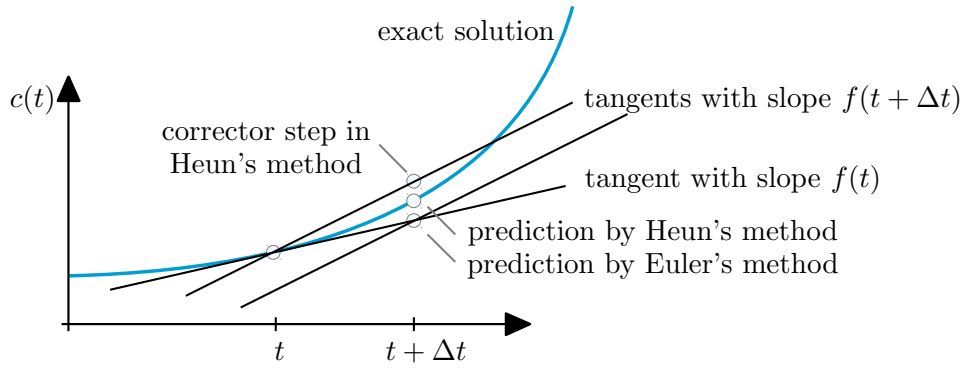

Figure 3.1: Comparison of the Euler and Heun's method for a simple one-dimensional ordinary differential equation $\frac{\partial c}{\partial t} = f(t)$.

One can show that the accuracy of this method is better than the accuracy of the Euler method, as the error decreases with $\mathcal{O}(\Delta t^2)$ for Heun's method rather than with $\mathcal{O}(\Delta t)$ for the Euler method. A geometric interpretation of Heun's method in comparison to the Euler method is shown in Fig. 3.1.

Just like the improvement from the Euler method to Heun's method, one can improve the latter by doing even more intermediate steps to have more interpolation points for a better approximation of the time step. This leads to a whole family of integration schemes, called Runge-Kutta (RK) methods. The general form of an explicit RK scheme is

$$c(\mathbf{x}, t+\Delta t) = c(\mathbf{x}, t) + \Delta t \sum_{i=1}^{s} \gamma_i k_i, \tag{3.6}$$

with the intermediate evaluations of the right-hand side

$$k_j = f\left(c(\mathbf{x}, t) + \Delta t \sum_{i=1}^{j-1} \beta_{ji} k_i,\ t + \alpha_i \Delta t\right). \tag{3.7}$$

The number of intermediate steps s denotes the so-called stage of the method. γ_i, α_i and β_{ji} are constants that can be calculated for any arbitrary s and also be tweaked for certain properties of the method. In general more stages lead to a higher accuracy, although the order of the method does not scale linearly with the stage s of the method for $s > 4$. A handy way to compile these constants are the so-called Butcher tableaus that are arranged as shown in table 3.1. A good overview over different Runge-Kutta schemes, especially the ones discussed here, can be found in [But08]. Obviously, the Euler and Heun's method presented earlier are just special Runge-Kutta methods with one and two stages, respectively.

Although the Runge-Kutta methods of a higher stage are in general more accurate than the Euler or Heun's method for a certain time step size Δt, we still need a method to find an actual number for Δt, that results in a stable method giving acceptable accurate results. Stable in this context means, that

0					
α_2	β_{21}				
α_3	β_{31}	β_{32}			
$\vdots$	$\vdots$	$\vdots$	$\ddots$		
α_s	β_{s1}	β_{s2}	$\cdots$	$\beta_{s\,s-1}$	
	γ_1	γ_2	$\cdots$	γ_{s-1}	γ_s

Table 3.1: Butcher tableau for a Runge-Kutta method of stage s.

truncation errors are bounded and do not lead to a possible divergence of the result from the true solution. One method to determine a time step size is the Courant-Friedrichs-Lewy condition [CFL28]. The basic idea behind this condition is that an imaginary particle at a certain grid point x_0 should travel no further than to one neighboring grid point $x_0+\Delta x$ in each time step, meaning

$$\Delta t < \frac{\Delta x}{u_{\max}}, \tag{3.8}$$

where $u_{\max}$ is the maximal velocity the imaginary particle can have. This can be calculated by the terms of the right-hand side. In one dimension, an advective term in the right-hand side, $v\frac{\partial}{\partial x}c$, for example delivers $u_{\text{adv}} = |v|$, a diffuse term $\nu\frac{\partial^2}{\partial x^2}c$ delivers $u_{\text{diff}} = \frac{\nu}{\Delta x}$. For the more-dimensional case, the contributions from each dimension have to be calculated separately and then added. The maximal velocity $u_{\max}$ is then the maximum over all u_{i} of all terms i of the right-hand side and over all grid points. For nonlinear terms, the estimated velocity is dependent on the actual state of the system and can therefore not be calculated a priori.

A different approach to find a value for the time step size Δt that is as large as possible (to reduce compute time) and as small as necessary (to have acceptable small errors) is to find an estimation for the truncation error ϵ made in each time step, compare it to a given, acceptable error size ϵ_{tol}, and then adjust the time step size accordingly to result in an error just below ϵ_{tol}. Because the time step size is then adapted in each step, such methods are called adaptive step size algorithms. The estimation of the error made in a step can be calculated by the difference in the results of two time steps, one with a nth-order Runge-Kutta method of stage s, and one with a $(n+1)$st-order Runge-Kutta method of stage $s+1$,

$$\epsilon = \left\| c(\mathbf{x}, t+\Delta t)_{\text{RK}_\text{n}} - c(\mathbf{x}, t+\Delta t)_{\text{RK}_{\text{n+1}}} \right\|. \tag{3.9}$$

The norm $\|\cdot\|$ can for example be defined as the maximum value over all grid points. If this error ϵ is smaller than the accepted error ϵ_{tol}, the time step is accepted and the next time step size will be increased. If $\epsilon > \epsilon_{\text{tol}}$, the step will be discarded and repeated with a decreased time step size. The optimal size can be calculated by the relation between ϵ and ϵ_{tol}, for example according to

$$\Delta t_{\text{new}} = \begin{cases} \beta \Delta t_{\text{old}} \left(\frac{\epsilon_{\text{tol}}}{\epsilon}\right)^{1/n} & \text{for } \epsilon > \epsilon_{\text{tol}} \\ \beta \Delta t_{\text{old}} \left(\frac{\epsilon_{\text{tol}}}{\epsilon}\right)^{1/(n+1)} & \text{for } \epsilon < \epsilon_{\text{tol}}, \end{cases} \tag{3.10}$$

where β is a "safety factor" in the range of $]0, 1]$, that ensures the error to stay well below the threshold [PTVF92]. It is chosen to be $\beta = 0.85$ in this thesis. This adaptive time step size algorithm is shown in Fig. 3.2.

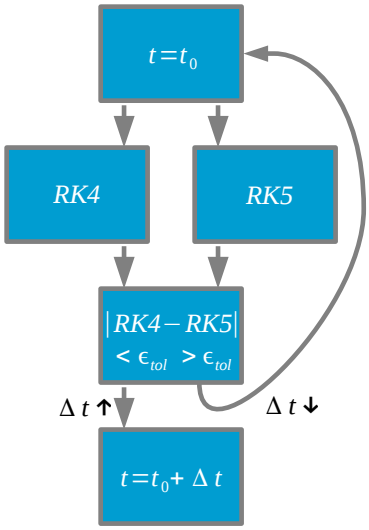

Figure 3.2: Flow diagram for the adaptive time step Runge-Kutta-Fehlberg method.

While this method always ensures a suitable choice of the time step size, it has the drawback to be numerically quite expensive, as it needs two full time steps of order n and $n + 1$ to be made in order to calculate the error ϵ. The effort for this can be reduced by so-called embedded algorithms that use shared stages k_i for both the nth- and $(n+1)$st-order algorithm. There exists a variety of different embedded Runge-Kutta methods [But08]. Probably the best known is the Runge-Kutta-Fehlberg method that uses a fourth-order ($n = 4,\ s = 5$) and a fifth-order ($n = 5,\ s = 6$) method. The corresponding Butcher tableau is shown in table 3.2. There are also other choices for the Runge-Kutta coefficients possible, for example those proposed by Dormand and Prince [But08], that will be used for two-dimensional simulations in this thesis, as they allow for slightly larger time step sizes. The coefficients are listed in table 3.3.

Obviously, besides the algorithm used for time integration, we still need a method to evaluate the right-hand side of our equation. In particular, we need to find a way to numerically deal with the differential operators.

3.2 Finite difference methods

There are many methods available that can be used to approximate the differential operators numerically for the evaluation of the right-hand side of a partial differential equation. Well known examples are spectral or pseudo-spectral methods and finite difference methods. The latter will be discussed and used here, because they allow for an easy implementation of specific boundary con-

0						
$\frac{1}{4}$	$\frac{1}{4}$					
$\frac{3}{8}$	$\frac{3}{32}$	$\frac{9}{32}$				
$\frac{12}{13}$	$\frac{1932}{2197}$	$-\frac{7200}{2197}$	$\frac{7296}{2197}$			
1	$\frac{439}{216}$	-8	$\frac{3680}{513}$	$-\frac{845}{4104}$		
$\frac{1}{2}$	$-\frac{8}{27}$	2	$-\frac{3544}{2565}$	$\frac{1859}{4104}$	$-\frac{11}{40}$	
	$\frac{25}{216}$	0	$\frac{1408}{2565}$	$\frac{2197}{4104}$	$-\frac{1}{5}$	
	$\frac{16}{135}$	0	$\frac{6656}{12825}$	$\frac{28561}{56430}$	$-\frac{9}{50}$	$\frac{2}{55}$

Table 3.2: Butcher tableau for the Runge-Kutta-Fehlberg method. The last two rows are the coefficients γ_i for the fourth-order method and the fifth-order method, accordingly.

0							
$\frac{1}{5}$	$\frac{1}{5}$						
$\frac{3}{10}$	$\frac{3}{40}$	$\frac{9}{40}$					
$\frac{4}{5}$	$\frac{44}{45}$	$\frac{-56}{15}$	$\frac{32}{9}$				
$\frac{8}{9}$	$\frac{19372}{6561}$	$-\frac{25360}{2187}$	$\frac{64448}{6561}$	$-\frac{212}{729}$			
1	$\frac{9017}{3168}$	$-\frac{355}{33}$	$\frac{46732}{5247}$	$\frac{49}{176}$	$-\frac{5103}{18656}$		
1	$\frac{35}{384}$	0	$\frac{500}{1113}$	$\frac{125}{192}$	$-\frac{2187}{6784}$	$\frac{11}{84}$	
	$\frac{32}{384}$	0	$\frac{500}{1113}$	$\frac{125}{192}$	$-\frac{2187}{6784}$	$\frac{11}{84}$	
	$\frac{5179}{57600}$	0	$\frac{7571}{16695}$	$\frac{393}{640}$	$-\frac{92097}{339200}$	$\frac{187}{2100}$	$\frac{1}{40}$

Table 3.3: Butcher tableau for the Dormand-Prince method. The last two rows are the coefficients γ_i for the fourth-order method and the fifth-order method, accordingly.

ditions needed in our model (2.22), and are straightforward to implement.

To understand the basic principle of the finite difference method, we start with a Taylor series expansion of a one-dimensional function $c(x)$ in the vicinity of the point x_0,

$$c(x_0 + \Delta x) = c(x_0) + \left.\frac{\partial c}{\partial x}\right|_{x_0} \Delta x + \frac{1}{2} \left.\frac{\partial^2 c}{\partial x^2}\right|_{x_0} \Delta x^2 + \mathcal{O}(\Delta x^3). \tag{3.11}$$

If we neglect all nonlinear terms and solve this equation for $\frac{\partial c}{\partial x}$, we obtain

$$\left.\frac{\partial c}{\partial x}\right|_{x_0} = \frac{c(x_0 + \Delta x) - c(x_0)}{\Delta x} + \mathcal{O}(\Delta x). \tag{3.12}$$

This means we can approximate the value of the derivative by the differential quotient, just like we did in the derivation of the Euler method. One can now combine such expressions to achieve a higher order of accuracy and to approximate higher derivatives. If we for example subtract (3.11) from the same equation for a step $-\Delta x$ backwards,

$$c(x_0 - \Delta x) = c(x_0) - \left.\frac{\partial c}{\partial x}\right|_{x_0} \Delta x + \frac{1}{2} \left.\frac{\partial^2 c}{\partial x^2}\right|_{x_0} \Delta x^2 + \mathcal{O}(\Delta x^3), \tag{3.13}$$

we end up with

$$\left.\frac{\partial c}{\partial x}\right|_{x_0} = \frac{c(x_0 + \Delta x) - c(x_0 - \Delta x)}{2\Delta x} + \mathcal{O}(\Delta x^2), \tag{3.14}$$

which is accurate up to order of $\mathcal{O}(\Delta x^2)$. We will now skip further derivations and just list the formulas that will be used. The interested reader is referred to [Smi86]. In the following, a short-hand notation just enumerating the positions on the discretized grid will be more convenient. We use $c_i := c(x_0)$, $c_{i+1} := c(x_0 + \Delta x)$, $c_{i-1} := c(x_0 - \Delta x)$, and so on. With this notation we obtain

$$\begin{aligned}
\left.\frac{\partial c}{\partial x}\right|_{x_0} &= \frac{c_{i+1} - c_{i-1}}{2\Delta x} + \mathcal{O}(\Delta x^2), \\
\left.\frac{\partial^2 c}{\partial x^2}\right|_{x_0} &= \frac{c_{i+1} - 2c_i + c_{i-1}}{\Delta x^2} + \mathcal{O}(\Delta x^2), \\
\left.\frac{\partial^4 c}{\partial x^4}\right|_{x_0} &= \frac{c_{i+2} - 4c_{i+1} + 6c_i - 4c_{i-1} + c_{i-2}}{\Delta x^4} + \mathcal{O}(\Delta x^2).
\end{aligned} \tag{3.15}$$

The coefficients that arise in these formulas can be memorized easier when writing them in form of stencils, like shown in Fig. 3.3. This concept can be easily extended to a function of two variables $c(x, y)$. We also use a shorter notation here, namely $c_i^j := c(x_0, y_0)$, $c_{i+1}^j := c(x_0 + \Delta x, y)$, $c_i^{j+1} := c(x_0, y_0 + \Delta y)$, and so on. The formulas for the Laplacian ∇^2 and the biharmonic operator

∇^4 then read

$$\nabla^2 c\big|_{x_0,y_0} = \frac{c_{i+1}^{j+1} + c_{i+1}^{j} + c_{i+1}^{j-1} + c_{i}^{j+1} - 8c_{i}^{j} + c_{i}^{j-1} + c_{i-1}^{j+1} + c_{i-1}^{j} + c_{i-1}^{j-1}}{3\Delta x^2} + \mathcal{O}(\Delta x^2), \tag{3.16}$$

$$\nabla^4 c\big|_{x_0,y_0} = \frac{1}{\Delta x^4}\Big(c_{i+2}^{j} + 2c_{i+1}^{j+1} - 8c_{i+1}^{j} + 2c_{i+1}^{j-1} + c_{i}^{j+2} - 8c_{i}^{j+1} + 20c_{i}^{j} - 8c_{i}^{j-1} + c_{i}^{j-2} + 2c_{i-1}^{j+1} - 8c_{i-1}^{j} + 2c_{i-1}^{j-1} + c_{i-2}^{j}\Big) + \mathcal{O}(\Delta x^2). \tag{3.17}$$

These formulas are also compiled in stencils in Fig. 3.4.

Obviously, the evaluation of finite difference schemes always necessitates the knowledge of surrounding grid points. However, there are always grid points on the boundary of the finite simulation domain that have no neighbors in one or even two directions. This problem can be either bypassed by the usage of asymmetric finite difference schemes, or by the introduction of virtual grid points, as it is described in the following.

3.2.1 Implementation of boundary conditions through virtual grid points

As already mentioned above, we have certain boundary conditions we want to apply to our system. For finite difference methods this can be achieved by introducing grid points lying just outside of the simulation domain, so that they are neighbors to the grid points at the boundary inside the simulation domain. The values of these grid points outside the simulation domain are set according to the boundary conditions to be met, and are not subject to our time integration. Therefore, they are called *virtual* grid points.

Let us consider the case of the lower boundary of our system (2.22),

$$c|_{x=0} = c_0 \quad \text{and} \quad \frac{\partial^2}{\partial x^2} c\bigg|_{x=0} = 0. \tag{3.18}$$

The first condition is obviously easy to implement by just setting $c_0^j = c_0$. For the implementation of the second condition we start with the finite difference expression for the second derivative at the lower boundary,

$$\frac{\partial^2 c}{\partial x^2}\bigg|_{i=0,j} = \frac{c_1^j - 2c_0^j + c_{-1}^j}{\Delta x^2} + \mathcal{O}(\Delta x^2). \tag{3.19}$$

By neglecting the higher order terms, we can solve this for the value of the lowermost row of virtual grid points c_{-1}^i,

$$c_{-1}^j = 2c_0^j - c_1^j + \frac{\partial^2 c}{\partial x^2}\bigg|_{i=0,j} \Delta x^2, \tag{3.20}$$

and by inserting the condition (3.18) we finally obtain

$$c_{-1}^j = 2c_0 - c_1^j. \tag{3.21}$$

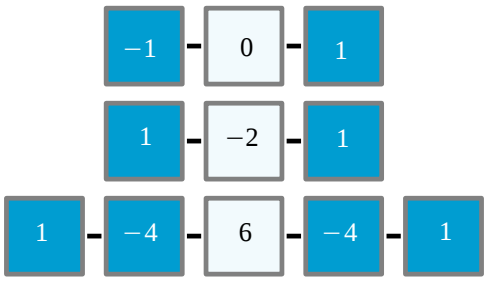

Figure 3.3: Stencils for the one-dimensional finite difference schemes with a second-order accuracy. From top to bottom are the stencils for the first, second and fourth derivative. The grid points at which the derivatives are evaluated are shown in light blue, while the neighboring grid points are colored dark blue.

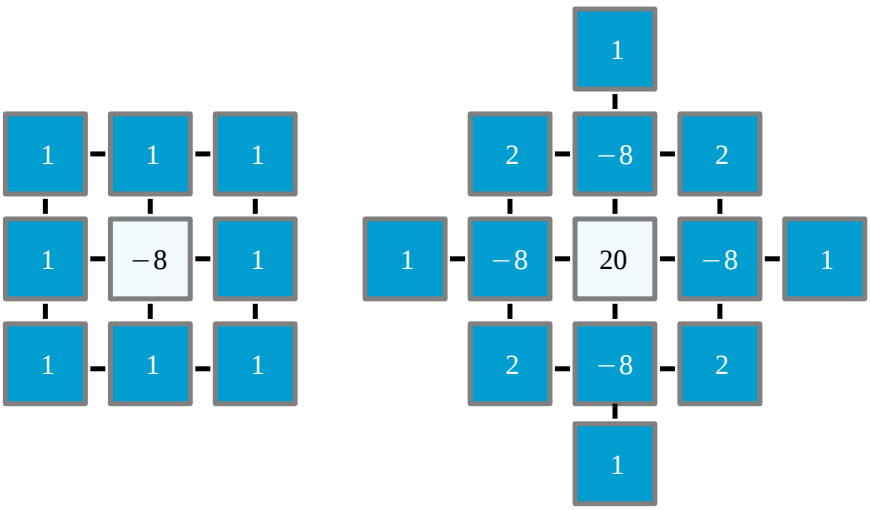

Figure 3.4: Stencils for the two-dimensional Laplacian (left) and biharmonic operator (right) difference schemes with a second-order accuracy. The grid points at which the derivatives are evaluated are shown in light blue, while the neighboring grid points are colored dark blue.

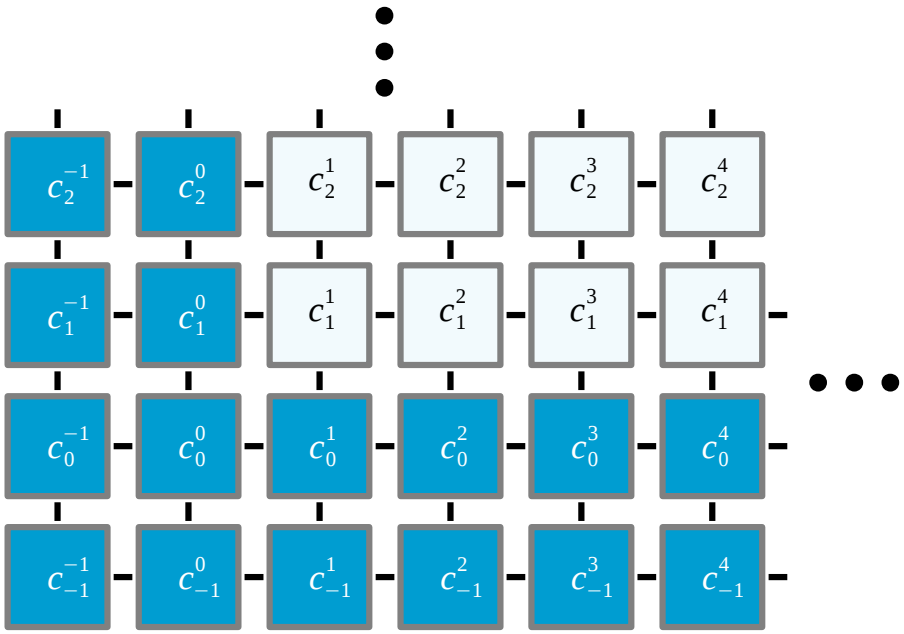

Figure 3.5: Sketch of the lower left corner of the simulation domain (light blue) and the neighboring virtual grid points to match the boundary conditions (dark blue).

For the implementation at the upper boundary, where we impose

$$\frac{\partial}{\partial x} c \bigg|_{x=L_x} = 0, \quad \text{and} \quad \frac{\partial^2}{\partial x^2} c \bigg|_{x=L_x} = 0, \tag{3.22}$$

the same approach can be used. We start with the forward finite difference schemes for the first and second derivative at the upper boundary, where $i = N_x$, the number of total of grid points in x direction. For the sake of simplicity, we assume a quadratic grid where $N_x = N_y := N$:

$$\frac{\partial c}{\partial x} \bigg|_{i=N_x,j} = \frac{c^j_{N+2} - c^j_N}{2\Delta x} + \mathcal{O}(\Delta x^2), \tag{3.23}$$

$$\frac{\partial^2 c}{\partial x^2} \bigg|_{i=N_x,j} = \frac{c^j_{N+2} - 2c^j_{N+1} + c^j_N}{\Delta x^2} + \mathcal{O}(\Delta x^2). \tag{3.24}$$

If we again drop the higher order terms, apply our conditions (3.22), and solve for the values of the virtual grid points, we end up with the simple condition

$$c^j_{N+2} = c^j_{N+1} = c^j_N, \tag{3.25}$$

fulfilling our imposed boundary conditions.

The periodic boundary conditions in y-direction can be easily implemented by making the left and right virtual points repeat the values at the right and left boundary accordingly,

$$c_i^0 = c_i^{N_y}, \quad c_i^{-1} = c_i^{N_y-1}, \quad c_i^{N+1} = c_i^1, \quad \text{and} \quad c_i^{N+2} = c_i^2. \tag{3.26}$$

So in summary, we have introduced virtual grid points outside our simulation domain and then determined their value by means of the boundary conditions we impose. This leaves us with additional grid points we can employ to evaluate the finite difference terms even at the boundary of our simulation domain, so we can use the same symmetric finite difference schemes for all grid points.

3.3 Parallelization for GPGPU

The time that a certain simulation run takes to finish depends on a variety of factors, like the speed of the processor, the number of grid points, the time step size and so on. Unfortunately, the time step size underlies the restriction of the Courant-Friedrichs-Lewy condition mentioned earlier. The fourth derivative in our model equation (2.22) simply necessitates quite small time step sizes. Also the number of grid points cannot be reduced too far if we want to simulate a certain system size with a satisfying resolution. This leaves the speed of the processor to tweak the simulation speed. In the last decades, the speed of the central processors in computers (CPU) rose almost exponentially as predicted by Moore's law [Rec06]. In the more recent past, this increase in computational power could not be accomplished by simply clocking processors faster, but only by adding more and more processing cores into one processor.

A different trend arose from the area of graphics processing units (GPU). These chips have always been designed to render millions of pixels in video games, a task that can be easily distributed to a lot of cores working simultaneously. Therefore, modern GPUs have hundreds to a few thousands of processing cores that have become available also for more general calculations through frameworks like CUDA [NVI] and OpenCL [SGS10]. This concept is called "General Purpose Computation on Graphics Processing Unit" (GPGPU). Because each core of a GPU is relatively slow compared to a core of a modern CPU, this technique is only reasonable for computations that can be parallelized easily into independently computable parts. Fortunately this is true for the finite difference method we want to employ. In fact, it can be parallelized down to the separate grid points, which means each GPU core is working on only one grid point. Of course, some communication between the cores is needed to exchange information about neighboring values for the evaluation of the finite difference formulas. In the CUDA framework each processing core is called *thread*, and a group of threads is called *block*. Such a block of threads has a shared memory, which is very fast and can be used to exchange the information. The speed of the shared memory is also what makes GPGPU interesting in comparison to parallelizing scientific software for conventional clusters of computers. Here the interconnect between the different memories of each node is slower compared to the communication between different blocks on one GPU. Therefore, GPGPU

qualifies for problems with a strong interdependence of all computing threads. This advantage of course drops out, as soon as more GPUs on different computing nodes should be employed. Nevertheless, the efficiency of GPGPU clusters is often higher than of conventional clusters, meaning they use less electrical power for the same amount of calculations.

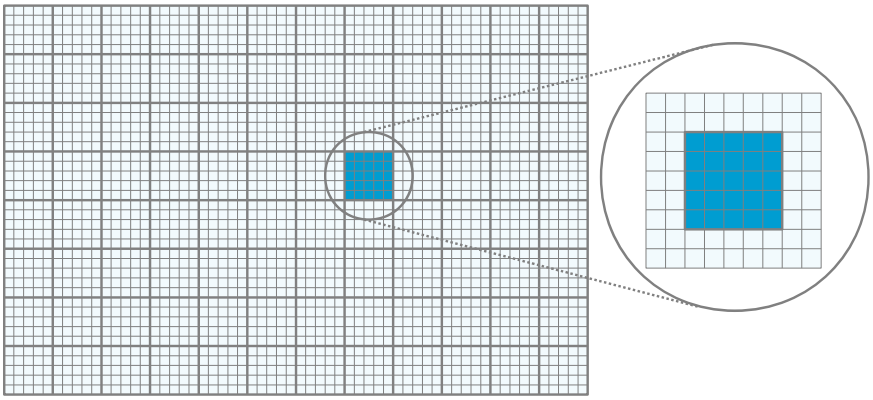

Figure 3.6: Sketch of the parallelization for the use of GPGPU. The whole domain is discretized into equidistant grid points, which are each calculated by one thread. A quadratic group of threads is combined to a block. Each block has a shared memory in which the information of its own thread and the next two neighbors are kept to evaluate the finite difference formulas.

The already mentioned memory layout makes programming for GPGPU different to what one is used to for classical CPUs. This is due to the fact that communication between the GPU and the system's main memory is much slower than between the GPU and the graphics memory. In addition, the communication of each thread with the shared memory of the associated block is again much faster. Therefore, one has to make sure all information needed for the threads to operate is kept as close as possible.

In our actual implementation, the memory is handled in the following way. The initial conditions for the simulation are either read from an input file or generated after a functional description by the main processor and are then accessible in the computer's main memory. Then they are copied to the graphics memory. The simulation domain is then divided into blocks of 16×16 threads, each of them responsible for one grid point. The threads of a block first copy the initial data of their grid points into the shared memory of the block, as well as the next two neighboring rows and columns of grid points. The computation of the different stages of each Runge-Kutta time step is then executed in parallel by all threads. After each stage, the results are copied back from the shared memory of the blocks to the graphics memory. This way the information needed for the next stage is distributed among all blocks. On the way, all threads have to be synchronized at certain times to ensure the integrity of the data, meaning no thread is running ahead of the others. The data in the graphics memory is only seldom copied to the computer's main memory for visualization or storage

for later analysis. The benefit for accounting for all these peculiarities are fast simulations, for example with a speedup of factor 10-20 in comparison to simulations on a CPU in our case (NVIDIA GeForce GTX 480 versus a Intel Core 2 Quad 9300).

3.4 The final numerical implementation

We want to summarize the methods we use for the numerical treatment of our nonlinear partial differential equation (2.22). We employ an embedded Runge-Kutta scheme of order 4(5) for the temporal integration of the initial value problem. The time step size is determined adaptively, ensuring the solution to stay below a threshold error in each time step. The evaluation of the differential operators on the right-hand side of the model equation (2.22) is accomplished with finite difference schemes. The boundary conditions imposed are implemented by the introduction of virtual grid points next to the grid points at the boundary of the simulation domain. The program was written in the programming language C++ and executed on desktop computers. Parameter studies have been distributed to the computers of the Morfeus GRID at the University of Münster, with the use of Condor [LLM88]. For two-dimensional simulations, the calculations were performed on modern graphics processors (NVIDIA GeForce GTX 480) using the CUDA framework, which provides extensions to C++ to access the graphics processor.

4 Transfer onto homogeneous substrates

From now on, we want to discuss results obtained by direct numerical simulations of our model. We start with the case of homogeneous substrates, that is, we assume the same strength of the SMC all over the substrate. In addition, we first focus on one-dimensional systems. Results in two dimensions will be discussed in Sec. 4.3.

4.1 Solution families in 1D

In the one-dimensional case, four qualitatively different types of solution of the model (2.22) exist. The transfer velocity v as the main parameter in the following considerations determines, which solutions are obtainable.

The first type of solution exhibits a steep increase in the concentration from the boundary value c_0 to a positive value near $c = 1$. At the location of the meniscus at $x_s = 10$, the onset of SMC yields a small corrugation. This type of solution is shown in Fig. 4.1. It is observable for a broad range of transfer velocities.

The second type of solution only exists for rather small transfer velocities and possesses a slight decrease in concentration until the onset of SMC, followed by a steep increase up to a positive value near $c = 1$. This corresponds to the transfer of a homogeneous layer in the LC phase, just like in the case of the first type of solution. A corresponding solution is shown in Fig. 4.2.

The third type of solution occurs only for higher transfer velocities. It shows the same decrease of concentration until the onset of SMC and an increase afterwards, just like solution type number two. But in contrast to this, the concentration then rises to a value near $c = -1$, corresponding to a homogeneous layer in the LE phase being transferred. Figure 4.3 shows such a solution. All these three types of solution are stationary and stable, meaning they do not change in time and are also insensitive to small perturbations.

The fourth type of solution is time-periodic. The solutions are characterized by domains of high concentration alternating with domains of low concentration, with each of them formed at the meniscus and then advected with the transfer velocity. This behavior corresponds to patterns of alternating domains in the LC and LE phase. Two examples of such solutions for different transfer velocities are shown in Figs. 4.4 and 4.5. The dependence of the occurring patterns on the transfer velocity will be discussed in the following section 4.2. To compare these solutions with experimental results, we can expand them uniformly in the y-direction. The solutions then describe the stripe patterns

perpendicular to the transfer direction, that are experimentally observed (see Fig. 1.4).

All these types of solution exist for a certain range of transfer velocities. Typically, for a given transfer velocity more than one type of solution is possible and therefore the initial conditions determine the solution type. In most simulations a smooth transition between $c(x = 0) = c_0$ and $c(x = L_x) = 1$ with a hyperbolic tangent shape was used as the initial condition. This type of initial condition favors the solution types 2 and 3 and the periodic solutions over the solution type 1 in the velocity ranges where they are possible. Therefore, the final states of simulations in the velocity range where only type 1 solutions are possible were used as initial conditions, too, to follow the branch of solutions of type 1 to higher transfer velocities.

A good overview over the possible solutions can be achieved by calculating the L^2-norm,

$$\|c(x)\|^2 = \frac{1}{L_x} \int_0^{L_x} c(x)^2 \, \mathrm{d}x, \tag{4.1}$$

where L_x is the system length. The results can then be combined for different transfer velocities and for all types of solution in an L^2 versus v diagram. There, each type of solution corresponds to a different solution branch. The result is shown in Fig. 4.6. It has to be noted that for the case of time-periodic solutions, the L^2-norm is averaged over time.

The results of the one-dimensional simulations presented in this section can be directly compared to the ones obtained in [KGFT12]. There, the same model Eq. (2.22) was investigated, and the same L^2 versus v diagram was obtained using a continuation technique. The comparison can be used as a good benchmark for the numerical implementation used in this thesis. It turns out that the branches of stable solutions obtained by the direct numerical simulations in this thesis resemble the findings of the continuation technique in [KGFT12]. Of course, the stationary, unstable solutions that could also be determined by means of the continuation technique could not be obtained with the direct numerical simulations used here. Because of the fact that the results obtained in this section equal the results found in the literature, we can be confident that our numerical implementation does not exhibit systematic errors.

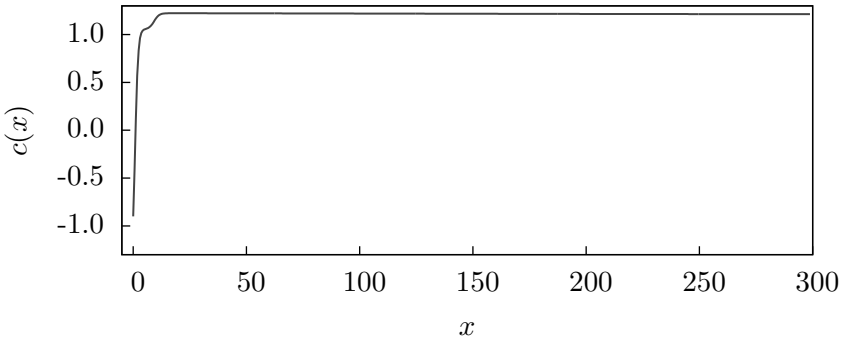

Figure 4.1: Stationary one-dimensional solution of Eq. (2.22) for $v = 0.015$, corresponding to the transfer of a layer in the LC phase.

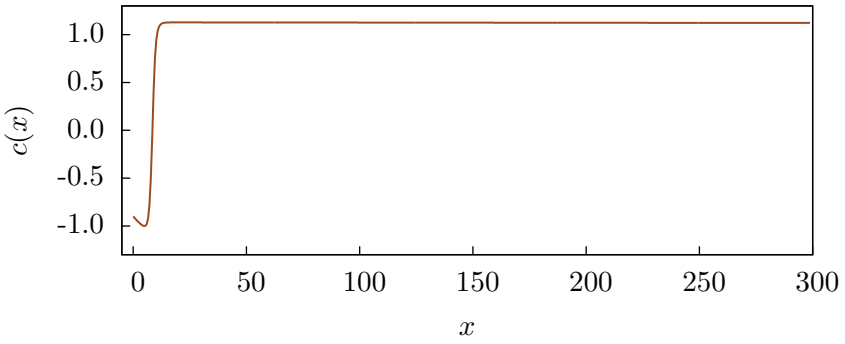

Figure 4.2: Stationary one-dimensional solution of Eq. (2.22) for $v = 0.02$, corresponding to the transfer of a layer in the LC phase.

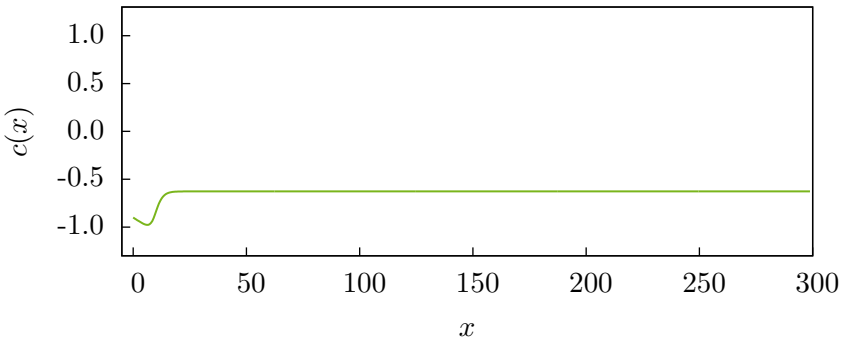

Figure 4.3: Stationary one-dimensional solution of Eq. (2.22) for $v = 0.08$, corresponding to the transfer of a layer in the LE phase.

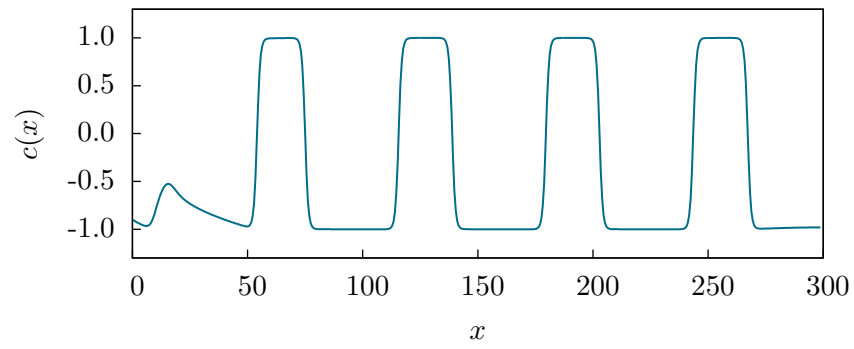

Figure 4.4: Snapshot of a periodic one-dimensional solution of Eq. (2.22) for $v = 0.04$, corresponding to the transfer of stripes in the LE and LC phase.

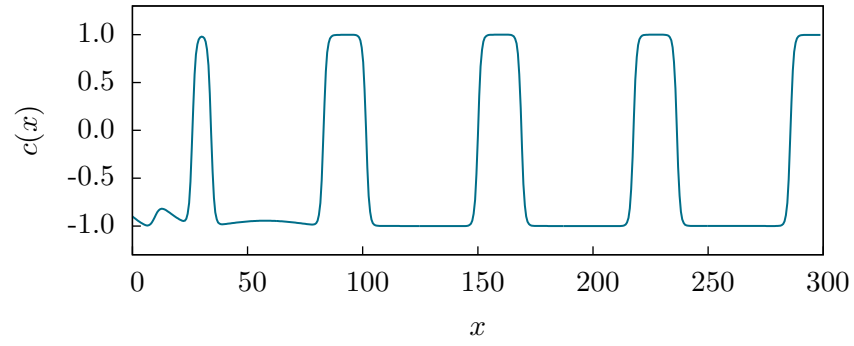

Figure 4.5: Snapshot of a periodic one-dimensional solution of Eq. (2.22) for $v = 0.05$, corresponding to the transfer of stripes in the LE and LC phase.

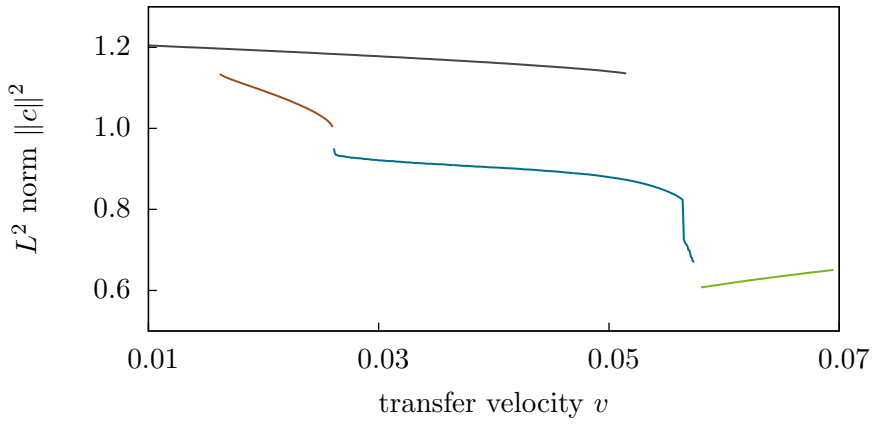

Figure 4.6: Branches of stable stationary and periodic solutions. The black line corresponds to stationary solutions of type 1 (see Fig. 4.1), the red line corresponds to stationary solutions of type 2 (see Fig. 4.2), the green line corresponds to stationary solutions of type 3 (see Fig. 4.3), whereas the blue line corresponds to time periodic solutions (see Figs. 4.4 and 4.5).

4.2 Periodic solutions in 1D

The periodic solutions we obtained can be best characterized by the wavenumber k and the duty cycle D of the resulting pattern. Figure 4.7 illustrates the definition of these quantities. The wavenumber results from the wavelength λ by $k = \frac{2\pi}{\lambda}$. The duty cycle is a measure for the ratio between the width l_{LC} of stripes in the LC phase and the wavelength, and therefore $D = \frac{l_{\mathrm{LC}}}{\lambda} \in [0, 1]$ is a reasonable definition.

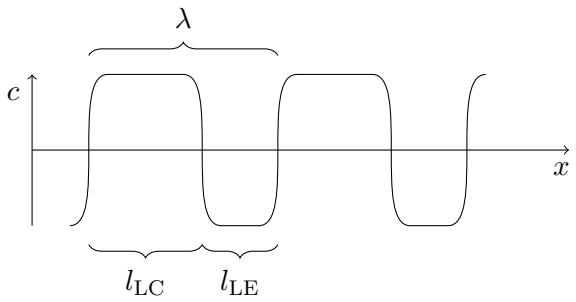

Figure 4.7: Sketch of the definition of the wavenumber $k = \frac{2\pi}{\lambda}$ and the duty cycle $D = \frac{l_{\mathrm{LC}}}{\lambda}$.

However, for the practical implementation, these definitions are slightly extended. We exploit the fact that after the formation of the stripes they are basically only advected with the transfer velocity v without changing their shape. Therefore, we can also measure the time $\Delta t_{\mathrm{stripe}}$ it takes for a stripe to pass a certain measurement location x_{m} and then calculate the corresponding wavelength as $\lambda = v \cdot \Delta t_{\mathrm{stripe}}$. This approach is easier to implement and has the advantage of a well-defined location for the measurement. The simulations presented in the following are performed for a system size $L = 300$ with $N = 500$ grid points.

We are now able to investigate the dependence of the properties of the periodic solutions in dependence of the transfer velocity. The results are shown in Fig. 4.8. Up to a velocity of $v = 0.0256 \pm 0.001$, no pattern formation occurs. At the onset of pattern formation, the wavenumber increases rapidly with v until a maximal value of k. The wavenumber then decreases for increasing v. Therefore, the same wavenumber can be achieved for different transfer velocities. However, the corresponding patterns are not identical as the duty cycle decreases monotonically with v for $v > 0.0277$. At the right end of the patterning regime, the curve $k(v)$ exhibits another small increase. The dynamics that leads to this behavior is rather complicated because with increasing v, the area where new stripes are formed is more and more carried away from the meniscus to the inside of the simulation domain. The simulations in this area show a very long transient behavior which necessitates simulations of sufficiently long times. The patterning stops, when the pattern forming area is carried outside the simulation domain. Therefore, the exact position of the upper boundary of the patterning regime is also dependent on the size of the simulation domain.

The simulations shown so far were performed with a fixed boundary value

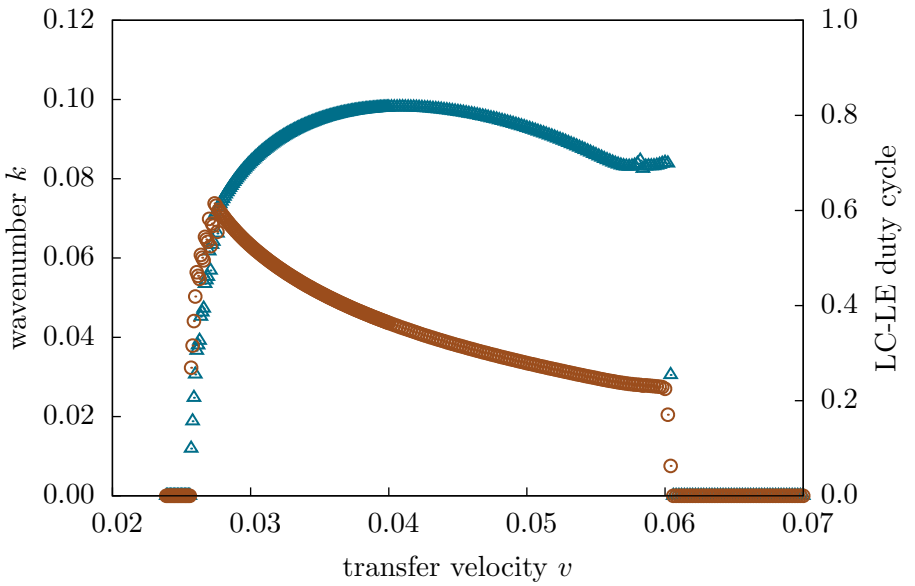

Figure 4.8: Wavenumber k (blue triangles) and duty cycle (red circles) of the occurring patterns in the periodic solutions in dependence of the transfer velocity v.

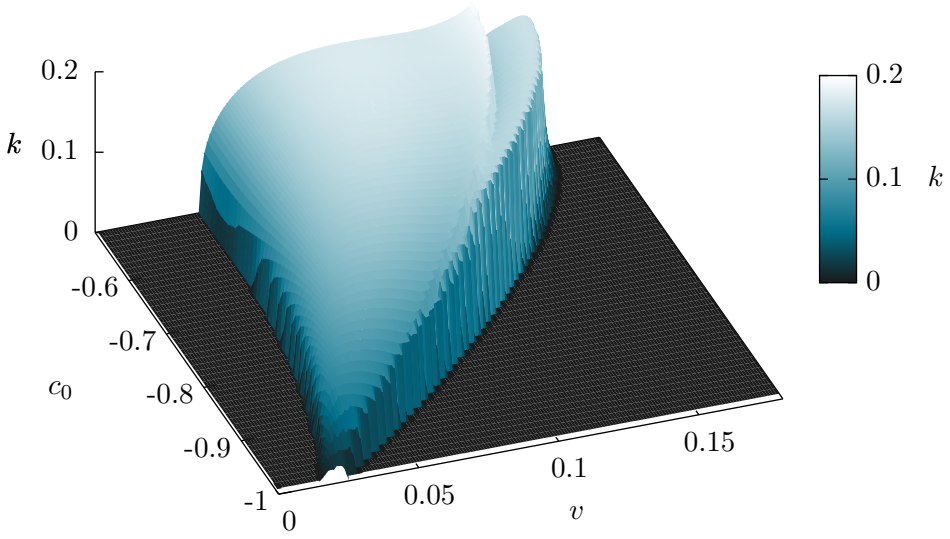

Figure 4.9: Wavenumber k of the occurring patterns in the periodic solutions in dependence of the transfer velocity v and the boundary concentration c_0.

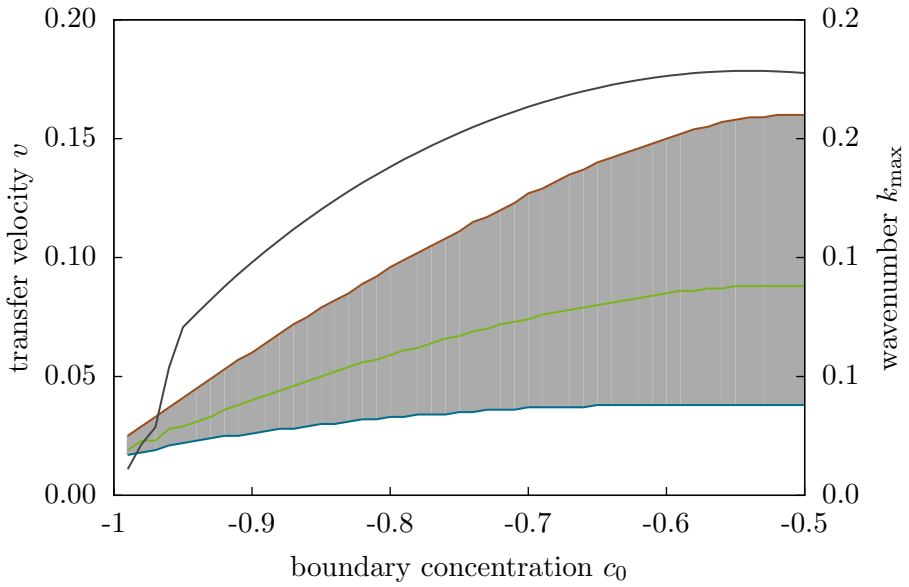

Figure 4.10: Upper (red line) and lower (blue line) boundary of the patterning regime in dependence of the boundary concentration c_0. The patterning regime between these boundaries is shown as a gray area. The green line depicts the position of the first local maximum of the curve $k(v)$. The corresponding maximal wavenumber $k_{\max}$ is shown as a gray line (with secondary ordinate).

of the concentration $c_0 = -0.9$. As this parameter influences the influx into the simulation domain significantly, we also want to study its influence on the patterning process. Figure 4.9 shows the dependence of the wavenumber k on the transfer velocity v and the boundary concentration c_0. Both the lower limit of the patterning regime and the upper limit are shifted toward higher velocities for increasing boundary concentrations. Because the upper limit is shifted further than the lower one, the patterning regime becomes larger with increasing c_0. Additionally, the maximal wavenumbers that can be achieved also increase, meaning the value of the local maximum in the middle of the patterning regime becomes larger. This result is interesting for experimental applications because it implies that smaller structures can be accomplished by increasing the boundary concentration. The boundaries of the patterning regime as well as the position and value of the wavenumber maximum are presented in Fig. 4.10. To obtain results that are comparable to the ones from the literature, we use a value of $c_0 = -0.9$ in the following.

4.3 Solutions in 2D

In general, all solutions we obtained in the one-dimensional case are also solutions in two dimensions if they are just extended homogeneously in the y-direction. This becomes immediately clear by looking at the model Eq. (2.22). Assuming a solution homogeneous in y-direction, all derivatives with respect

to y vanish and one is left with the one-dimensional version of the equation. Therefore, the one-dimensional solutions have to be solutions in two dimensions, too. As it will be discussed later on, such pseudo two-dimensional solutions do not have to be necessarily stable with respect to perturbations in y-direction. An example of such a solution that is indeed stable is shown in Fig. 4.11. The concentration of the monolayer $c(x, y)$ is color-coded with red areas referring to the high density LC phase and blue areas referring to the low density LE. The transfer process occurs from bottom to top, meaning the meniscus is located at the bottom and the substrate is pulled in the top direction.

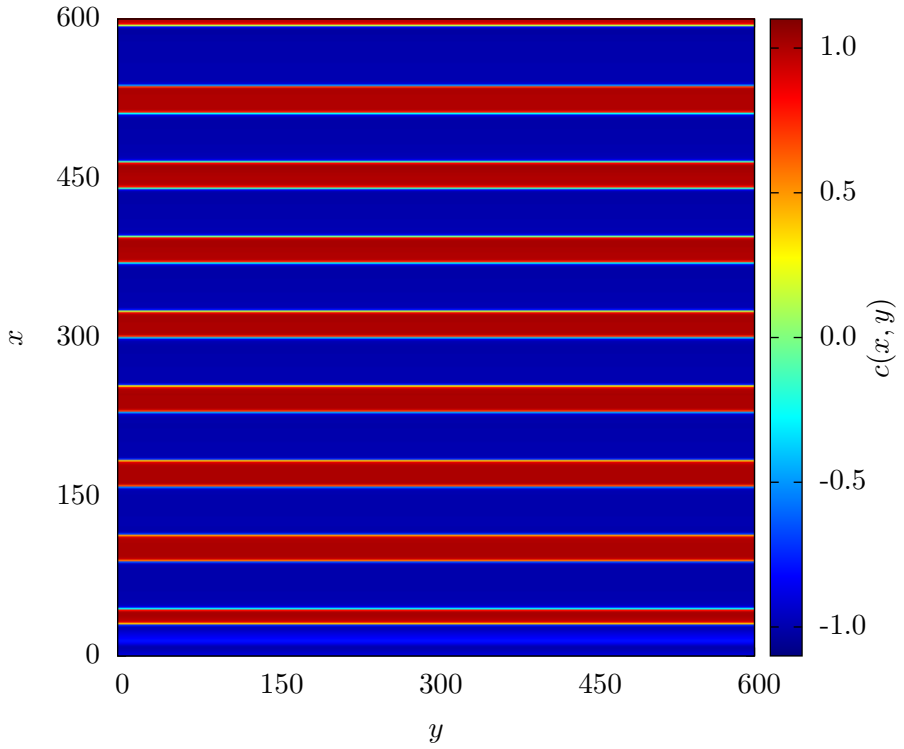

Figure 4.11: Snapshot of a two-dimensional simulation with a domain size of $L_x \times L_y = 600 \times 600$ with $N_x \times N_y = 384 \times 384$ grid points and a transfer velocity of $v = 0.04$. The solution is homogeneous in y-direction and therefore identical to the one-dimensional solution.

More interesting are of course truly two-dimensional simulations which also show variation in y-direction. One example is shown in Fig. 4.12, where the occurrence of stripes perpendicular to the liquid meniscus is shown. Such solutions can be obtained for low transfer velocities in the patterning regime. This behavior resembles the findings of experimental studies, see, for example, Fig. 1.4 and [CLH+07]. This type of stripes appears after a secondary instability after the formation of stripes parallel to the meniscus. This will be investigated further by means of a linear stability analysis in chapter 6. In

order to induce an instability of this type, one has of course to introduce some kind of inhomogeneity in the y-direction, e.g., by slightly perturbing the initial conditions with additive noise, or varying the spatial location of the meniscus x_s with respect to y.

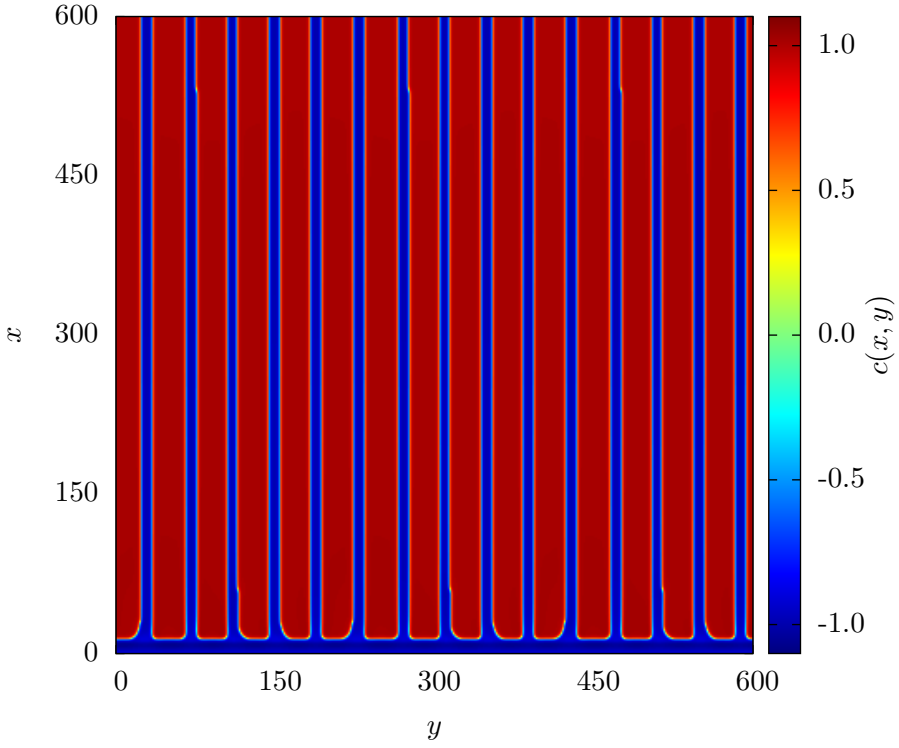

Figure 4.12: Snapshot of a two-dimensional simulation with a domain size of $L_x \times L_y = 600 \times 600$ with $N_x \times N_y = 384 \times 384$ grid points and a transfer velocity of $v = 0.03$. The stripes are now oriented perpendicular to the liquid meniscus.

A visualization of the temporal buildup of perpendicular stripes is presented in Fig. 4.13, showing a time series of snapshots of a simulation with a low transfer velocity $v = 0.03$. At the beginning, stripes parallel to the meniscus are formed, but they then become unstable and exhibit gaps in the y-direction. The areas of high concentration beside the gaps then expand in the x-direction, tending to form stripes perpendicular to the meniscus. After a few of such processes, the simulation domain is filled with perpendicular stripes. The wavelength in y-direction is yet not necessarily the one preferred by the system and therefore changes slowly by the creation of defects, for example by merging or splitting of stripes.

The relaxation time to a stationary state can be very long. In this transient phase, the system tries to optimize its configuration by introducing defects. Figure 4.14 shows a time series of snapshots illustrating a scenario. In the first

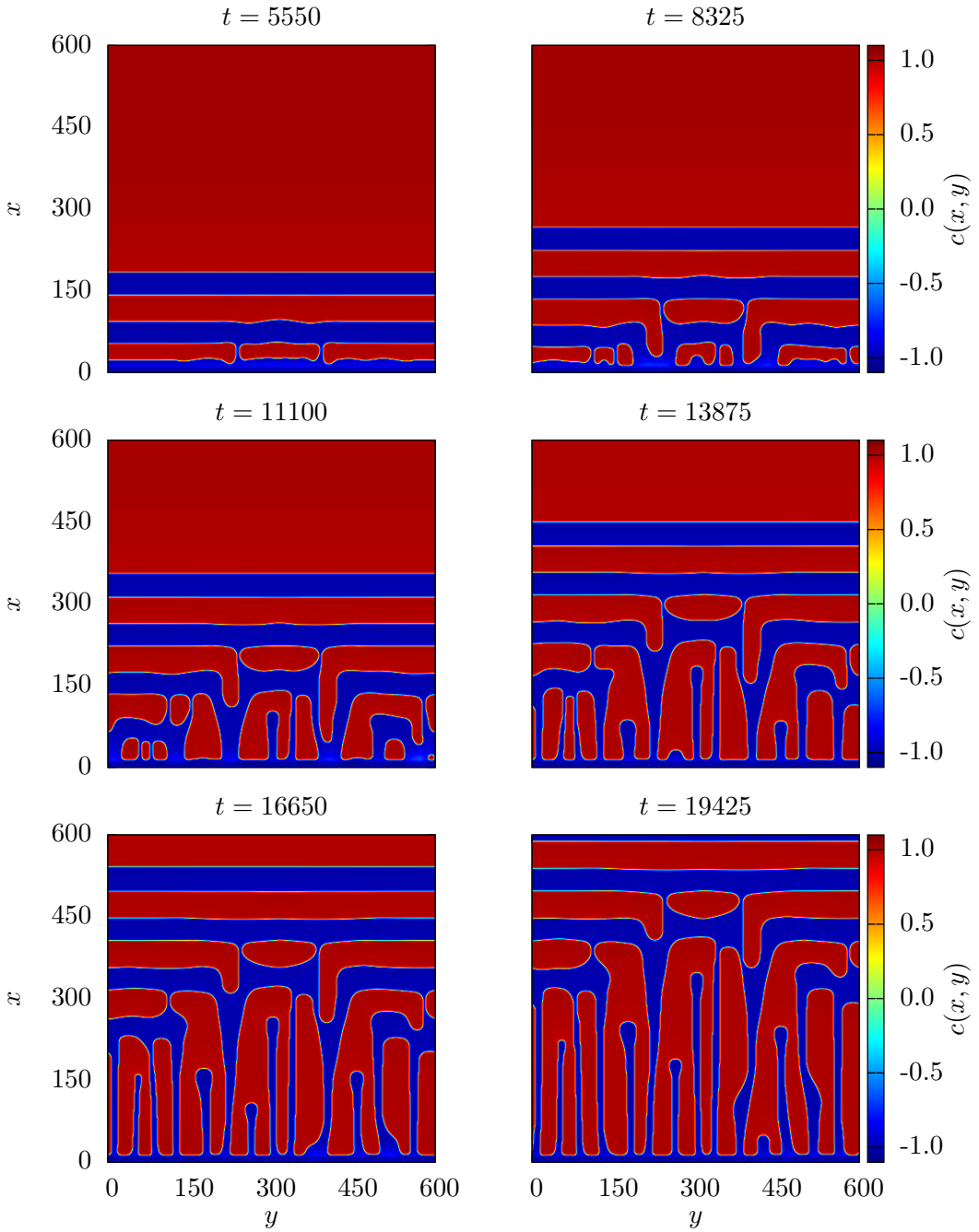

Figure 4.13: Time series of snapshots of a two-dimensional simulation showing the transition between stripes parallel to the meniscus to stripes perpendicular to the meniscus. The same parameters as in Fig. 4.12 were employed.

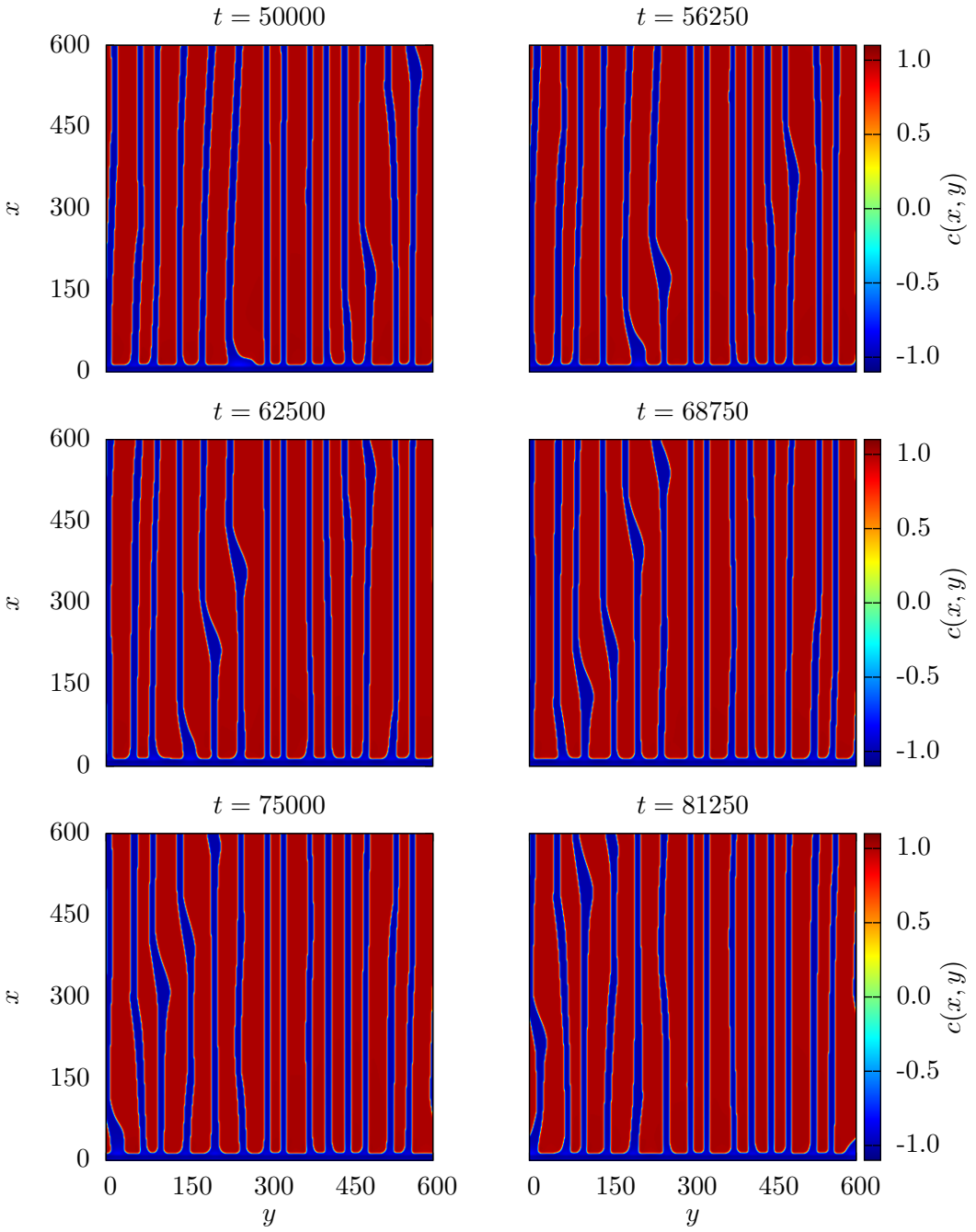

Figure 4.14: Time series of snapshots of a two-dimensional simulation showing the creation of defects in the stripe patterns. The same parameters as in Fig. 4.13 were employed, however, the snapshots show the evolution at a later time t.

snapshot ($t = 5 \cdot 10^4$), the sixth stripe from the left is broader than the rest and therefore suddenly thins out to a more preferred width, leaving more space for the neighboring fifth stripe. This stripe then spreads out to fill the new space, but afterward also again thins out to its preferred width. This leaves more space for the fourth stripe, and so on. Hence, as a result, some kind of defect wave is traveling in a transverse direction, leaving the stripes behind it with more preferred stripe widths.

In such a scenario, the boundary conditions at the left and right of the simulation domain become important. As we impose periodic boundary conditions, we implicitly introduce this additional symmetry to the solutions obtained with these simulations. This can of course conflict with the natural solution the system would develop in the absence of boundaries, for example if the system would prefer a y-periodicity λ, while the system size L_y is no integer multiple of this periodicity. The system is then forced to a slightly different periodicity or to the formation of defects. This leads to solutions that never become stationary, but for example exhibit traveling defects, like shown in Fig. 4.14. Such defects can be seen in analogy to, e.g., the zigzag instability in the Swift-Hohenberg equation [CH93].

4.4 Langmuir-Blodgett rotating transfer

In the following section, we want to make a little excursion to a slightly different transfer process called Langmuir-Blodgett rotating transfer, as it has been investigated similarly in [CHFC07]. This technique allows for the production of gradient structures where, for example, stripes are oriented like a fan. Such structures can occur when stripes parallel to the meniscus are formed and then advected with a rotational movement of the substrate, which is the essential difference to the conventional Langmuir-Blodgett transfer. While up to now we only considered a straight, linear transfer upward with a constant transfer velocity $\mathbf{v}$, we now assume the transfer to happen onto a substrate that is rotated around a hinge located outside the trough. A sketch of this experimental setup is shown in Fig. 4.15.

This approach has basically three implications for our model of the transfer process. As a first consequence, the transfer velocity now also has a component in y-direction, that is, in the direction of the meniscus. In addition, the absolute value of the transfer velocity is not constant across the substrate, but varies with the distance from the rotation center. Furthermore, the boundary conditions at the left and the right boundaries cannot be assumed to be periodic anymore, because this would conflict with the transfer velocity that is no more translational invariant. Instead, we apply the same boundary conditions to the left and right boundary that we already use for the upper boundary. That is, we impose vanishing first and second derivatives at the boundaries,

$$\left.\frac{\partial}{\partial y} c\right|_{y=0} = 0, \quad \left.\frac{\partial^2}{\partial y^2} c\right|_{y=0} = 0, \quad \left.\frac{\partial}{\partial y} c\right|_{y=L_y} = 0, \quad \left.\frac{\partial^2}{\partial y^2} c\right|_{y=L_y} = 0. \tag{4.2}$$

For the simulations of LB rotating transfer, we use a slightly changed setup

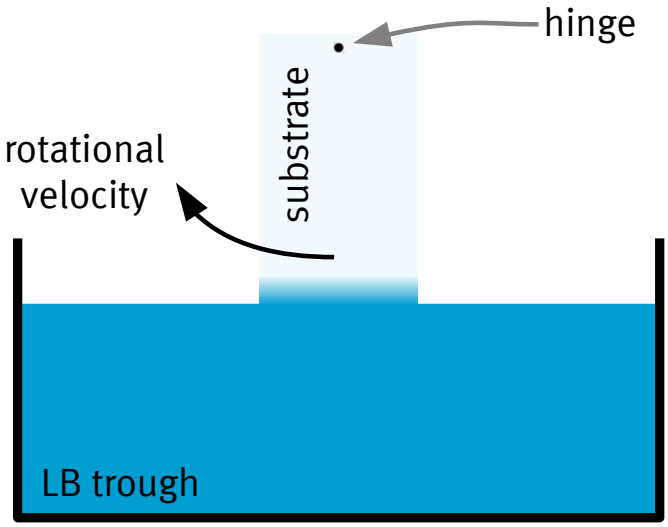

Figure 4.15: Illustration of the experimental setup for Langmuir-Blodgett rotating transfer.

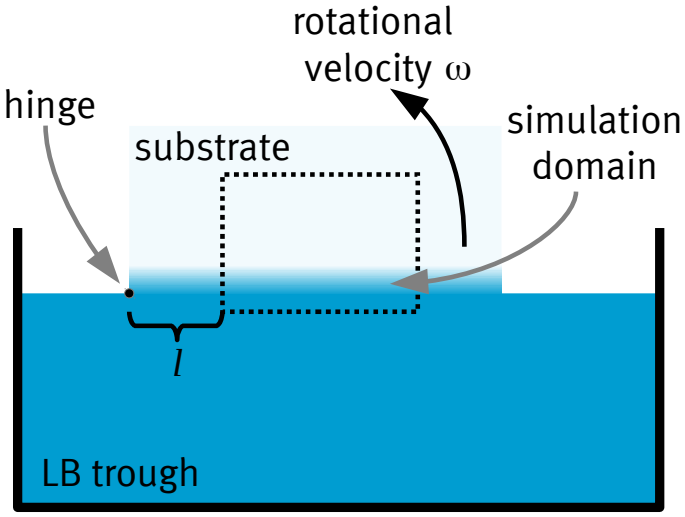

Figure 4.16: Illustration of the setup used for numerical simulations of Langmuir-Blodgett rotating transfer.

that is shown in Fig. 4.16. The only difference to the experimental setup used in [CHFC07] is the location of the rotation center, which we assume to be on the liquid surface, and not above the trough. This configuration is advantageous for simulations because there exist no parts of the substrate being pushed into the trough, which could conflict with the boundary conditions used for the lower boundary.

Considering this setup, we now essentially have two new parameters describing the transfer process, i.e., the rotational velocity ω of the substrate, and the distance l between the rotation center and the simulation domain (see Fig. 4.16). Both parameters influence the shape of the velocity field $\mathbf{v}(x, y)$ via the simple relations

$$v_x(x, y) = \omega\, r(x, y) \cos\left(\alpha(x, y)\right), \quad \text{and} \tag{4.3}$$

$$v_y(x, y) = -\omega\, r(x, y) \sin(\alpha(x, y)), \quad \text{with} \tag{4.4}$$

$$r(x, y) = \sqrt{(y + l)^2 + x^2} \quad \text{and} \quad \alpha(x, y) = \arctan\left(\frac{x}{y + l}\right).$$

A sketch of a velocity vector field given by Eqs. (4.3)-(4.4) is shown in Fig. 4.17.

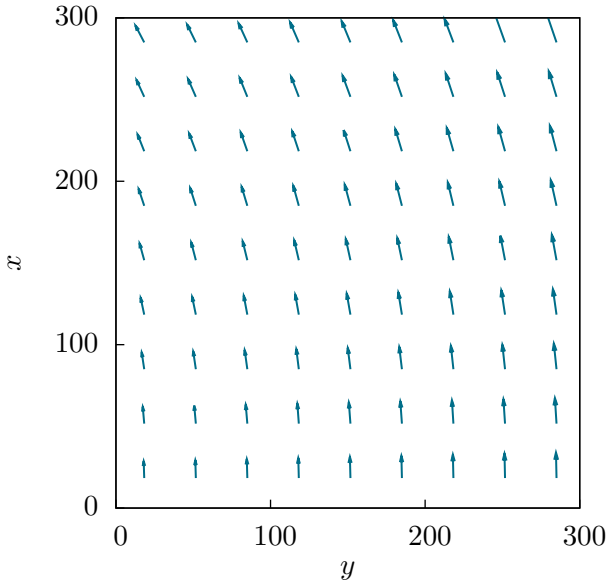

Figure 4.17: Sketch of the velocity vector field $\mathbf{v}(x, y)$ given by Eqs. (4.3)-(4.4) for Langmuir-Blodgett rotating transfer at a distance $l = 500$ from the rotation center.

The results obtained in [CHFC07] basically show that the patterning process at the meniscus in principle does not change because the authors still observe stripes that are formed parallel to the meniscus, and then carried away with the movement of the substrate. Because of the rotation, the stripes are not parallel to each other, but form a gradient mesostructure. To investigate this process in theory, we employ simulations of the rotating transfer for different distances

l between the simulation domain and the rotation center. The rotational frequency ω was adjusted in a way that the x-component of the velocity is kept constant to $v_x = 0.05$ at the center of the lower boundary $(0, L_y/2)$. The angle α between the stripes and the meniscus was measured using the software package GIMP at the position $(300, 400)$ after a simulation time $T = 8000$, where we assume an uncertainty of one degree. An example of such a simulation for $l = 4000$ including a sketch clarifying the definition of α is shown in Fig. 4.18.

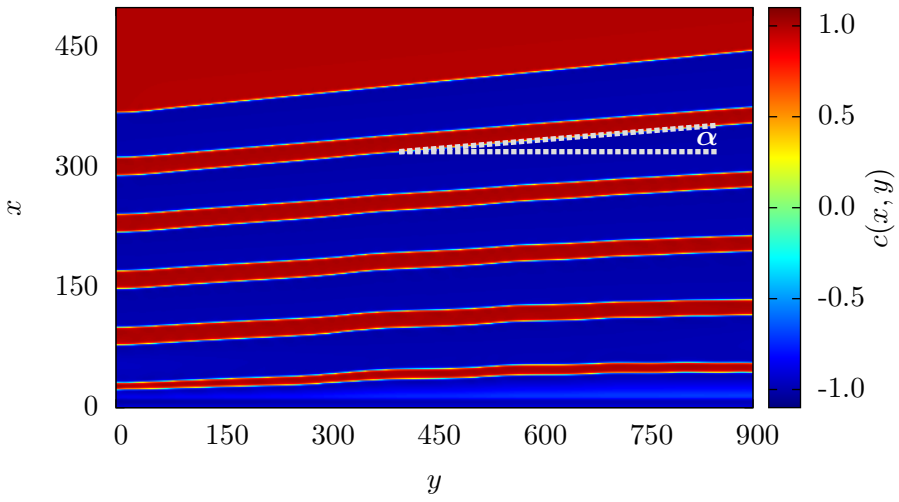

Figure 4.18: Snapshot of a simulation of Langmuir-Blodgett rotating transfer at a distance of $l = 4000$ from the rotation center. Stripes parallel to the meniscus are formed and then advected non-uniformly, leading to a certain angle α between the resulting stripes and the meniscus.

Under the assumption that the stripes are indeed only advected with the rotational velocity field, the angle α of the stripes can of course be easily calculated by geometrical considerations, i.e.,

$$\alpha(x, y) = \arctan\left(\frac{x}{y + l}\right). \tag{4.5}$$

This theoretical expectation along with the results obtained by the numerical simulations is shown in Fig. 4.19, and it obviously resembles the data from the simulations very well, as well as the experimental results from [CHFC07].

Besides in situations where the gradient structures formed by LB rotating transfer are really needed for a certain application, this technique can also be applied in other cases. An example are situations where a certain property should be examined for different transfer velocities. While in conventional LB transfer this would necessitate the repetition of the experiment for different velocities, one experiment with LB rotating transfer can be sufficient because different areas on the substrate are subject to different transfer velocities, depending on their distance to the rotation center.

This can also be achieved by LB rotating transfer simulations as it is shown in Fig. 4.20. Because the distance to the rotation center was chosen to be

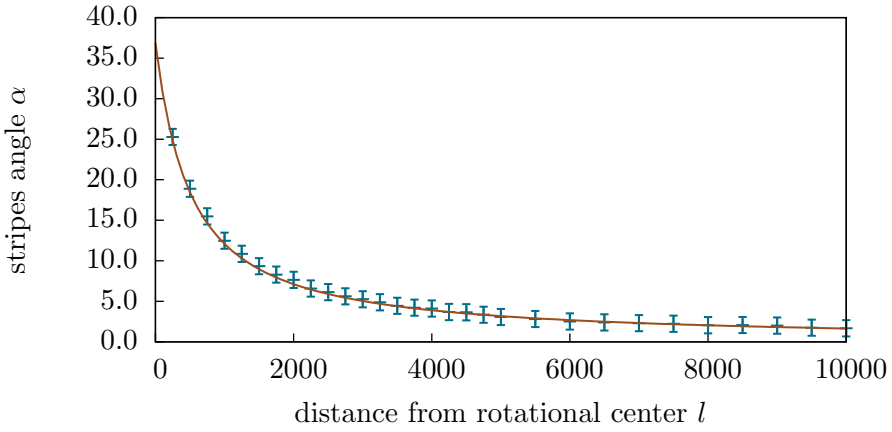

Figure 4.19: Dependence of the angle α of the stripes at the position $(400, 300)$ on the distance l of the rotation center. The data obtained by numerical simulations (blue points with error bars) resemble the theoretical expectation (red line).

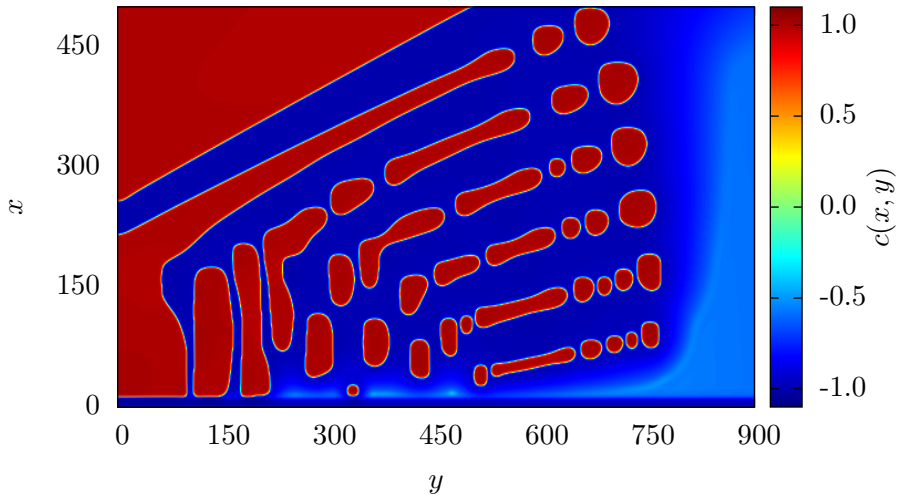

Figure 4.20: Snapshot of a two-dimensional simulation of Langmuir-Blodgett rotating transfer at a distance of $l = 500$ from the rotation center. The velocity in x-direction at the meniscus ranges from $v_x = 0.023$ at the left boundary to $v_x = 0.064$ at the right boundary, covering a range where all types of transfer during normal Langmuir-Blodgett transfer are observed: homogeneous transfer of a LC layer, stripes perpendicular to the meniscus, stripes parallel to the meniscus, and homogeneous transfer of a LE layer (from left to right). The defects of the stripes parallel to the meniscus occur due to the strong velocity gradients in this area.

quite small with $l = 500$ in this simulation, there is a large transfer velocity gradient across the simulation domain. The velocities at the meniscus therefore cover a range from $v_x = 0.023$ at the left boundary to $v_x = 0.064$ at the right boundary, which includes the whole patterning regime (see Fig. 4.8). That is, in just one simulation, we can see the transfer of a homogeneous LC phase, of stripes perpendicular to the meniscus, of stripes parallel to the meniscus, as well as the transfer of a homogeneous LE phase (from left to right) simultaneously.

After this short excursion to Langmuir-Blodgett rotating transfer, we want to come back to the case of linear transfer. In contrast to the considerations up to now, we want to focus on substrates with a chemical prestructure, which introduces a spatially varying strength of the substrate-mediated condensation.

5 Transfer onto prestructured substrates

Besides the transfer onto homogeneous substrates, also the transfer of a monolayer onto a substrate that has some kind of prestructure is conceivable. In addition to the effects discussed above, the monolayer transfer then is influenced by an inhomogeneity of a certain parameter, e.g., the wettability of the substrate. This of course opens up a new possibility to control the transfer process, which also has been experimentally realized [GHLL99]. The prestructure on the substrate can, for example, be produced by lithographic processes, or just by means of a Langmuir-Blodgett transfer itself [QXX+99].

As a prestructure influences the interaction between the substrate and the monolayer, it can be incorporated as a spatial variation of the strength of the SMC. We only want to focus on spatially periodic prestructures because they give rise to interesting synchronization phenomena. Such effects can occur if one considers a system with a natural, inherent frequency, like the transfer process in the patterning regime, that is coupled to an external forcing with a possibly different, external frequency, like a periodic prestructure. We again start with the investigation of the one-dimensional case.

5.1 Incorporation of prestructured substrates into the model

Up to now, the spatial dependence $\zeta(x)$ of the SMC was modeled as a smooth transition from no influence of the SMC to a certain fixed value after the meniscus at position x_s,

$$\zeta(x) = -\frac{1}{2}\left(1 + \tanh\left(\frac{x - x_\mathrm{s}}{l_\mathrm{s}}\right)\right). \tag{5.1}$$

We generalize the function $\zeta(x)$ by introducing a spatial modulation $m(x,t)$ of the value of the SMC after the meniscus,

$$\zeta(x,t) = -\frac{1}{2}\left(1 + \tanh\left(\frac{x - x_\mathrm{s}}{l_\mathrm{s}}\right)\right) \cdot (1 + \rho \cdot m(x,t)). \tag{5.2}$$

Here ρ is a scalar factor determining the strength or the *contrast* of the prestructure. A value of $\rho = 0$ would correspond to the case of no prestructure, while increasing ρ means an increasing difference in the strength of SMC between different regions on the substrate. Typically, we choose ρ to be in the range of a few percent, while $m(x,t) \in [-1,1]$. For the form $m(x,t)$ of the modulation we use a smooth transition between alternating domains of higher

and lower SMC in x-direction, mimicking stripes on the prestructured substrate parallel to the meniscus,

$$m(x,t) = \tanh\left(a\left(4\left|\mathrm{frac}\left(\frac{x-vt}{L_{\mathrm{pre}}}\right)-0.5\right|-1\right)\right). \tag{5.3}$$

Here, L_{pre} denotes the periodicity of the prestructure, a is a measure for the steepness of the transition between domains of different values of the SMC, and frac() is the fractional function, returning the fractional part of its argument. For L_{pre}, different values of the same order of magnitude as the natural wavelength inside the patterning regime have been used. The value of a was chosen as $a = 10$. Snapshots of the curve $\zeta(x,t)$ for different times t and for different prestructure contrasts ρ are shown in Fig. 5.1.

As one would expect, the effect of the prestructure is governed by the contrast ρ, resulting in little to no influence on the patterning process for very low values of ρ. But in addition to ρ, the periodicity L_{pre} does also play an important role. If L_{pre} on the one hand is much larger than the natural wavelength of the system, the transfer process occurs basically like on a homogeneous substrate, distorted only seldom by the transitions between different values of the SMC. On the other hand, prestructures with a very short periodicity L_{pre} introduce a forcing to the system that is much faster than the timescale the system can react on. In this case, the system only feels the average value of the SMC, but not the fast fluctuations. Therefore, the most interesting effects can be expected for values of L_{pre} of the same order of magnitude as the natural wavelength of the system. In this case, synchronization can occur, meaning the wavenumber k of the occurring patterns has a well-defined fractional relation to the wavenumber $k_{\mathrm{pre}} = \frac{2\pi}{L_{\mathrm{pre}}}$ of the prestructure, and the phase relationship between both patterns is locked to a well-defined value.

5.2 Synchronization with prestructures in 1D

First, we want to consider the one-dimensional case. We employ the same parameters used in Sec. 4.2 and additionally apply a prestructure with $L_{\mathrm{pre}} = 60$ and varying contrasts up to $\rho = 0.03$. Three examples for different velocities and a contrast $\rho = 0.012$ are shown in Figs. 5.2–5.4. The solution in Fig. 5.2 exhibits a 1:1 synchronization between the occurring pattern and the prestructure, meaning both wavelengths are equal. For a higher transfer velocity, a 2:3 synchronization can occur, as shown in Fig. 5.3. The pattern that is transferred in this case does not have one distinct wavelength, but two that alternate in a way, that they add up to three wavelength of the prestructure. The average wavenumber of the pattern is then equal to two thirds of the prestructure wavenumber. For an even higher transfer velocity, the wavelength of the transferred pattern is uniformly twice the wavelength of the prestructure, referring to a 1:2 synchronization (see Fig. 5.4).

This synchronization behavior can be conveniently examined in a k versus v diagram, as shown in Fig. 5.5, where the k axis is normalized to the wavenumber k_{pre} of the prestructure. Therefore, the synchronization ratio can be directly

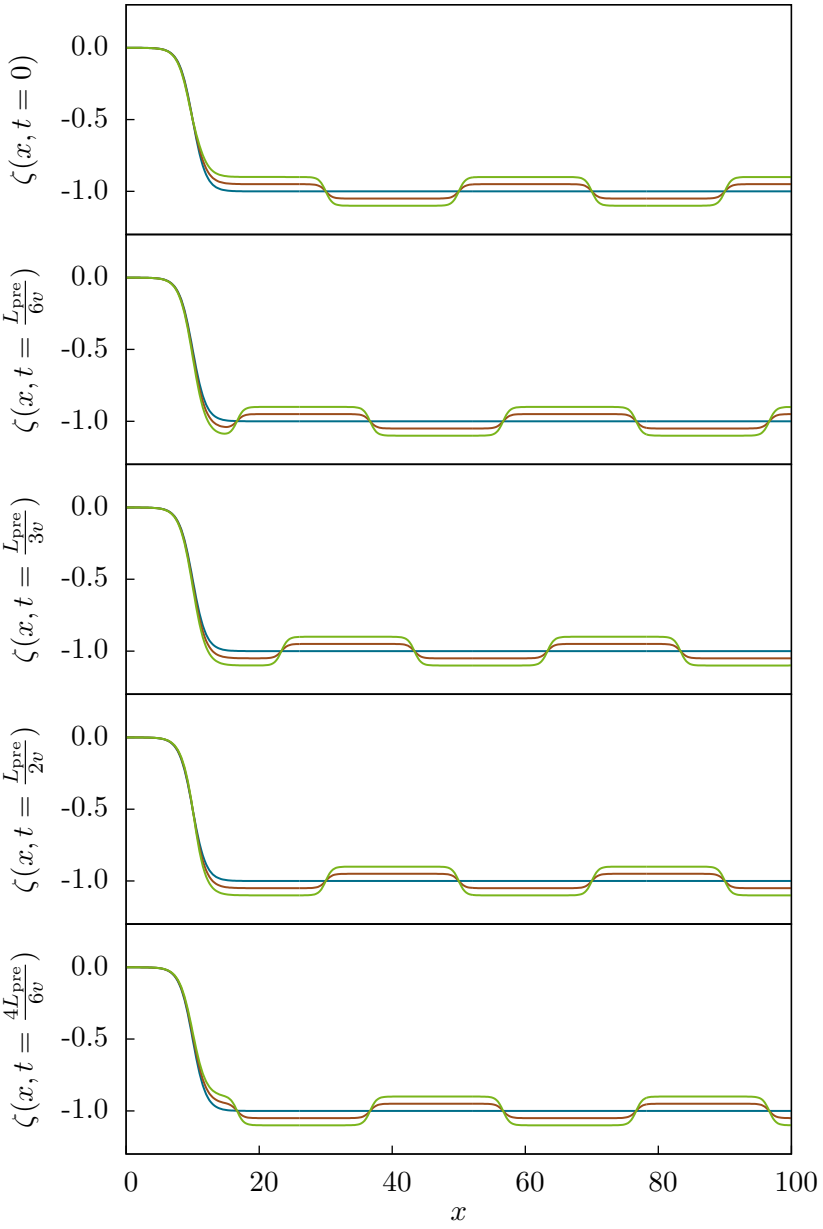

Figure 5.1: Spatial and temporal evolution of the function $\zeta(x, t)$ for a prestructured substrate with $L_{\mathrm{pre}} = 40$. The different colors refer to different prestructure contrasts: $\rho = 0$ (blue line), $\rho = 0.05$ (red line), $\rho = 0.1$ (green line). The temporal evolution is shown in snapshots for increasing time t from top to bottom.

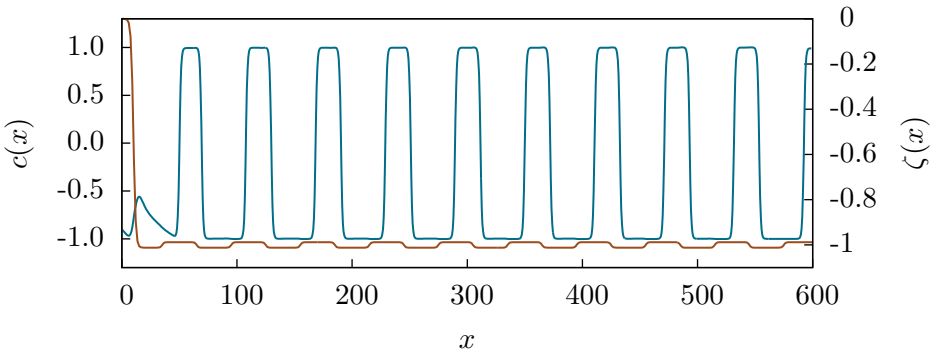

Figure 5.2: Snapshot of the periodic solution of Eq. (2.22) for $v = 0.04$ on an prestructured substrate with $L_{\text{pre}} = 60$ and $\rho = 0.012$. The solution (blue line) exhibits a 1:1 synchronization with the prestructure $\zeta(x)$ (red line).

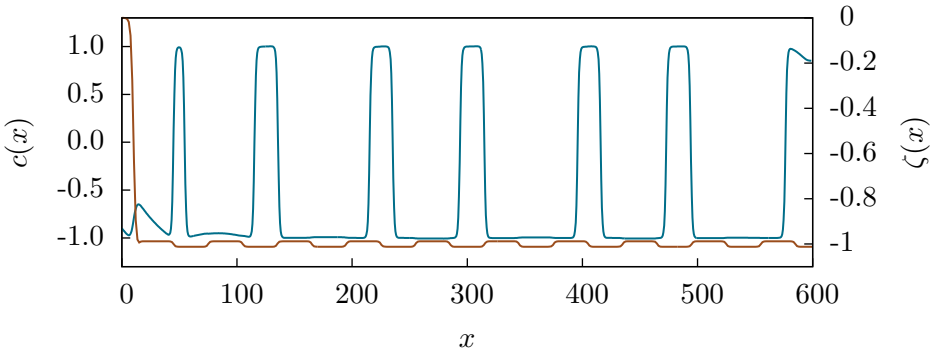

Figure 5.3: Snapshot of the periodic solution of Eq. (2.22) for $v = 0.06$ on an prestructured substrate with $L_{\text{pre}} = 60$ and $\rho = 0.012$. The solution (blue line) exhibits a 2:3 synchronization with the prestructure $\zeta(x)$ (red line).

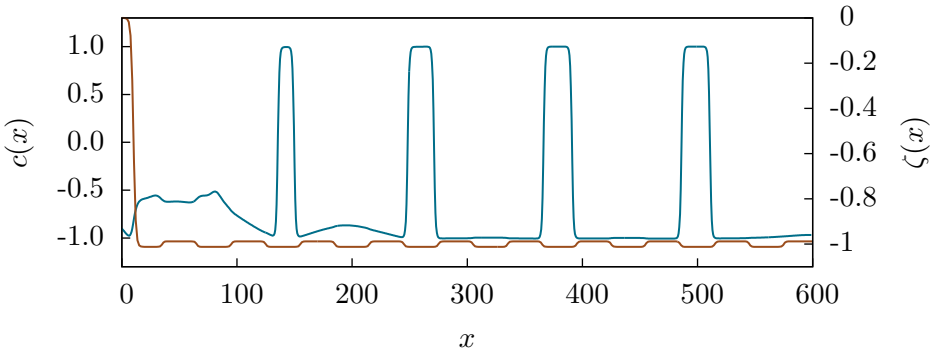

Figure 5.4: Snapshot of the periodic solution of Eq. (2.22) for $v = 0.07$ on an prestructured substrate with $L_{\text{pre}} = 60$ and $\rho = 0.012$. The solution (blue line) exhibits a 1:2 synchronization with the prestructure $\zeta(x)$ (red line).

read off the ordinate. Synchronization regimes can be identified as intervals on the abscissa with nearly constant wavenumber. As one would expect, the synchronization regimes grow for increasing prestructure contrast ρ.

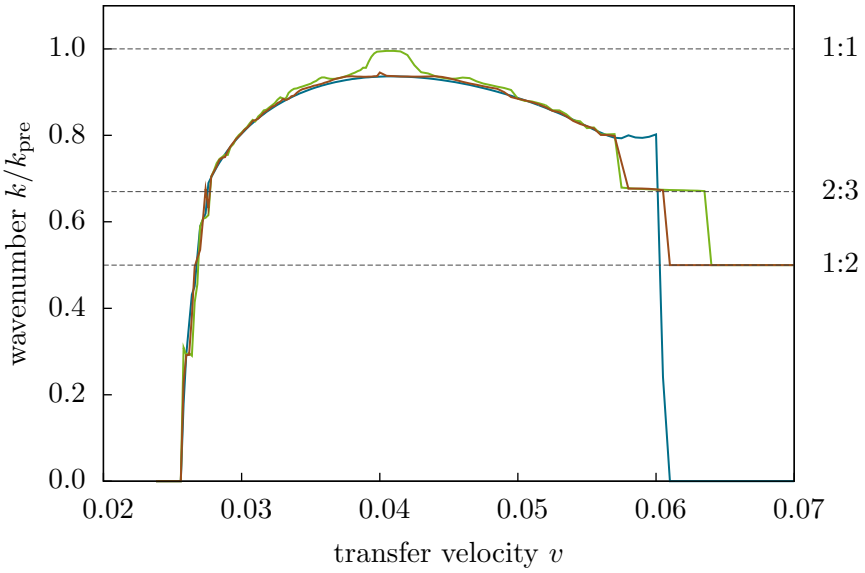

Figure 5.5: Wavenumber k of the occurring patterns in the periodic solutions of Eq. (2.22) in dependence of the transfer velocity v for different prestructure contrasts $\rho = 0$ (blue line), $\rho = 0.006$ (red line), and $\rho = 0.010$ (green line). The wavenumber has been normalized to the wavenumber of the prestructure $k_{\mathrm{pre}} = 2\pi/L_{\mathrm{pre}}$ with $L_{\mathrm{pre}} = 60$.

Additionally, two effects of a prestructured substrate can be observed in Fig. 5.5: The patterning regime is enlarged toward higher transfer velocities to an extent that grows with increasing prestructure contrast. Therefore, a patterned transfer is possible on prestructured substrates even for velocities that lead to a homogeneous transfer in the LE phase on homogeneous substrates. As a second effect, a prestructure can induce patterns with a higher wavenumber than the ones the system achieves on a homogeneous substrate. This can be observed in Fig. 5.5 for a prestructure contrast of $\rho = 0.01$, where the maximal wavenumber is shifted upwards to a 1:1 synchronization. In the experimental context, this means the minimal wavelength of the stripes can be reduced by the use of prestructured substrates.

A good overview over the synchronization behavior for different prestructure contrasts can be achieved by concentrating only on the synchronization regimes and compiling them in a contrast ρ versus transfer velocity v diagram. Figure 5.6 (top) shows such a diagram for a prestructure wavelength $L_{\mathrm{pre}} = 60$. Here, the colored areas depict the regions in the ρ–v–plane where synchronization occurs, while each color refers to a different synchronization ratio. Because of their shape, the regions are called *Arnold tongues* [PRK03], named after the Russian mathematician Vladimir Arnold (1937-2010). Especially the broaden-

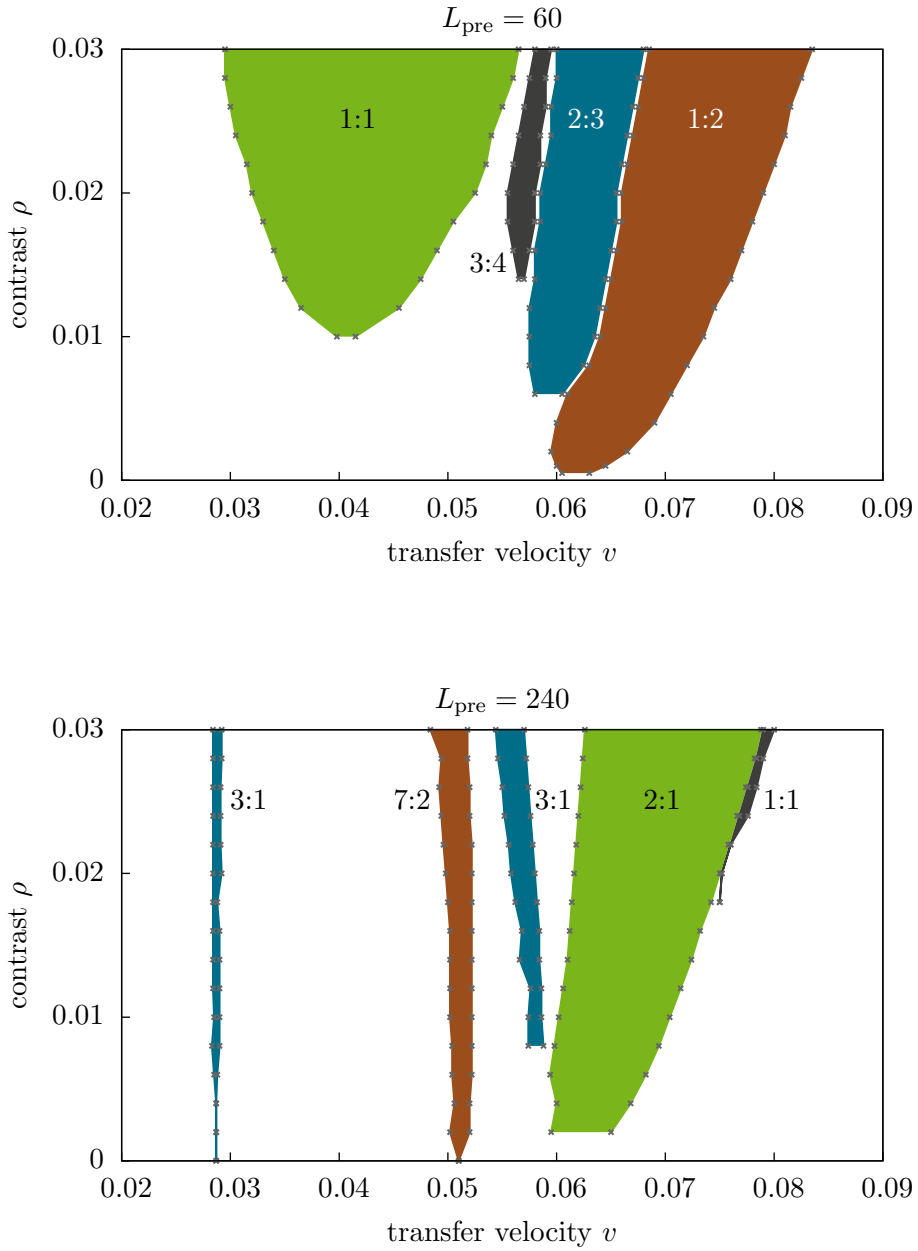

Figure 5.6: Arnold diagrams showing the areas of synchronization with a prestructure with $L_{\mathrm{pre}} = 60$ (top) and $L_{\mathrm{pre}} = 240$ (bottom). Different synchronization ratios are shown as different colors. The diagrams can be read from bottom to top to read off the contrast ρ, after which a new area of synchronization occurs.

ing of the synchronization regimes for increasing contrast ρ can be directly read off such a diagram.

As mentioned before, the prestructure wavelength L_{pre} also has an important influence on the synchronization behavior. To illustrate this, Fig. 5.6 (bottom) shows the same Arnold diagram like Fig. 5.6 (top), but for a prestructure wavelength $L_{\mathrm{pre}} = 240$. In this case, the natural wavelength of the system is typically shorter than the one of the prestructure. Therefore, synchronization ratios above 1:1 now occur, like, e.g., 2:1 or 3:1, which means two or three wavelengths of the occurring pattern now sum up to one wavelength of the prestructure.

The results of this section can be seen in comparison to the ones obtained in [KGF11], where the Langmuir-Blodgett transfer onto prestructured substrates was investigated in the framework of the full model we briefly introduced in chapter 1. Just like in our case, the full model exhibits synchronization phenomena with prestructures, and similar synchronization diagrams like the ones in Fig. 5.6 were obtained, revealing the characteristic Arnold tongues. Therefore, it is notable, that the easier Cahn-Hilliard model used in this thesis is obviously sufficient to investigate the synchronization phenomena with prestructured substrates.

As a result, we can summarize that prestructured substrates can be a powerful way to control the patterning process. Especially the facts, that the patterning regime can be expanded toward higher velocities, and that the maximal wavenumber possible can be increased, are remarkable as they extend the experimental possibilities.

5.3 Effects of prestructures in 2D

Just as in the case of homogeneous substrates, the same effects that were observed in one dimension can also trivially occur in two dimensions if one only extends the one-dimensional solution homogeneously into the new y-direction. An example is shown in Fig. 5.7, where a snapshot of a two-dimensional simulation is presented. The solution exhibits a 1:2 synchronization, just like in the one-dimensional case in Fig. 5.4. Because the effects are equivalent to the ones discussed previously for the one-dimensional case, we want to focus on new effects in the following.

Figure 5.8 shows an AFM image of a DPPC monolayer transferred onto a prestructured substrate. The prestructure can be identified as the five broad stripes perpendicular to the transfer direction in the right half of the image. Obviously, more complex patterns occur in the presence of the prestructure. The occurring pattern exhibits stripes that are bended toward the boundaries of the prestructure. It is still unclear, what kind of dynamics leads to such patterns. For a numerical simulation with our model, some difficulties hinder us from exactly reproducing the experimental results. At first, it is challenging to find a good estimation for the contrast ρ in our model that corresponds to the properties of the experimental prestructure. Another difficulty is given by the dimensions involved in the experimental setting. The width and wavelength of the prestructure in the experiment are much larger than the wavelength

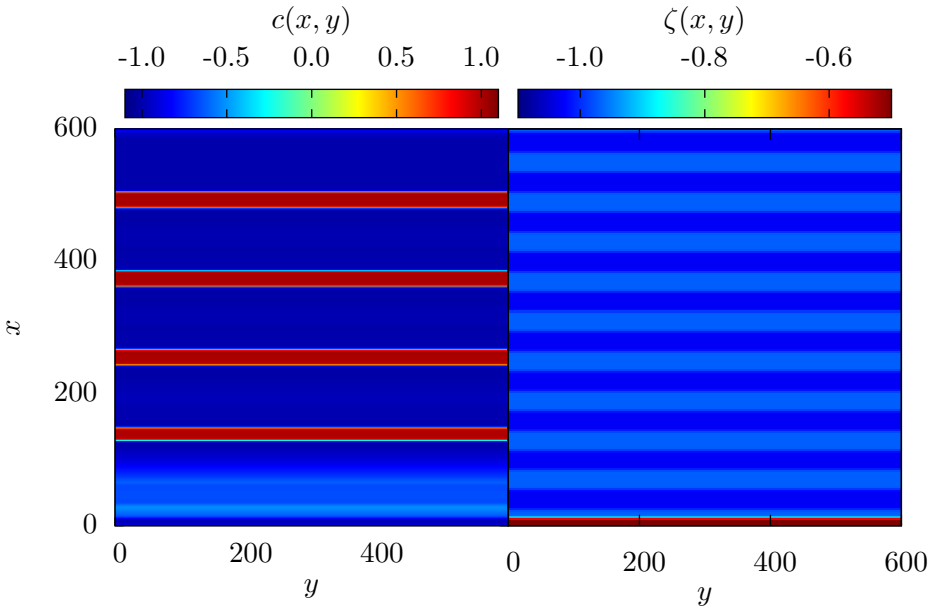

Figure 5.7: Snapshot of a two-dimensional simulation of the transfer with $v = 0.07$ onto a prestructured substrate with $\rho = 0.03$ and $L_{\text{pre}} = 60$. The solution (left) exhibits a 1:2 synchronization with the prestructure (right).

of the occurring pattern. Therefore, a large simulation domain with still a fine resolution in the grid is needed to resolve both the occurring pattern and the prestructure. Third, the resulting patterns can raise the speculation, that possibly the bended stripes occurred due to a liquid meniscus receding *perpendicular* to the transfer direction, which would contradict the assumption of a frozen meniscus in our model.

Nevertheless, the model is still capable to exhibit similar effects, concerning the bending of stripes. Such a simulation is shown in Fig. 5.9. Here, the transfer onto a prestructured substrate with $L_{\text{pre}} = 400$ is simulated. The stripes of the prestructure are oriented parallel to the meniscus, just like in the case simulated in one dimension in the previous section. But in contrast to this, the prestructure in this case is not present across the entire domain in y-direction, but only for $y \in [500, 2500]$. Therefore, the system is not exposed to the prestructure at the left and right boundary. Exactly at these transitions from prestructure to no prestructure, the solution exhibits bending of the occurring stripe patterns. While Fig. 5.9 only showed a section of the simulation domain to clarify the shape of the stripes near the onset of the prestructure, Fig. 5.10 covers the whole domain.

Although these results do not fully explain the experimental findings, they still resemble some aspects of them. Therefore, we are confident, that our model can also be used to simulate the transfer onto substrates with more complex prestructures, enabling also more complex patterning control.

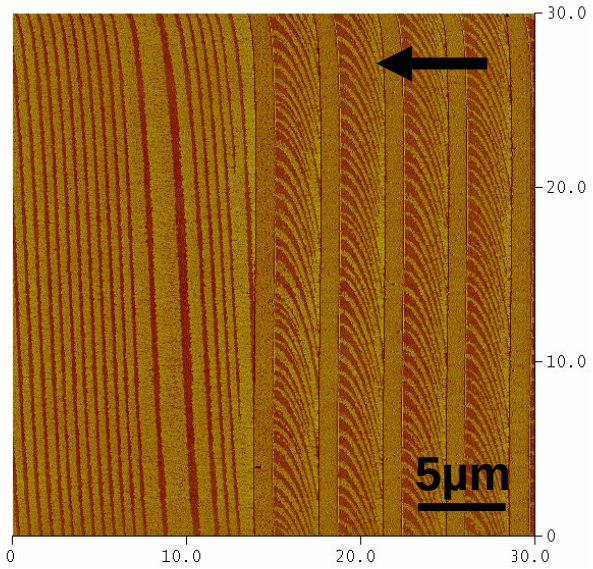

Figure 5.8: AFM image of the occurring pattern of DPPC in the LE and LC phase after Langmuir-Blodgett transfer onto a prestructured substrate. The black arrow depicts the transfer direction. Taken from [HL10].

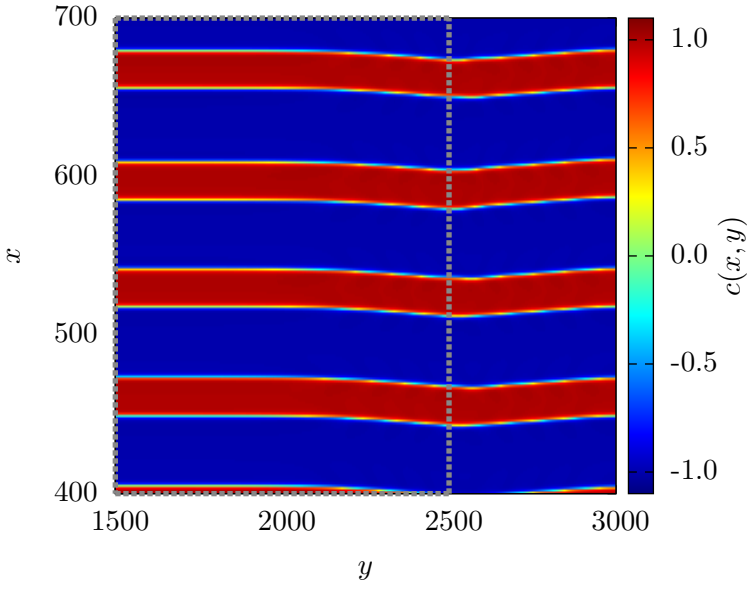

Figure 5.9: Snapshot of a two-dimensional simulation, where the transfer onto a prestructured substrate is simulated. The prestructure consists of stripes with $L_{\text{pre}} = 400$ that reach from $y = 500$ to $y = 2500$ (depicted by the gray dashed lines). The solution exhibits bending of the occurring stripes at the boundary of the prestructure stripes. The figure is an enlargement of the upper right corner of the simulation shown in Fig. 5.10.

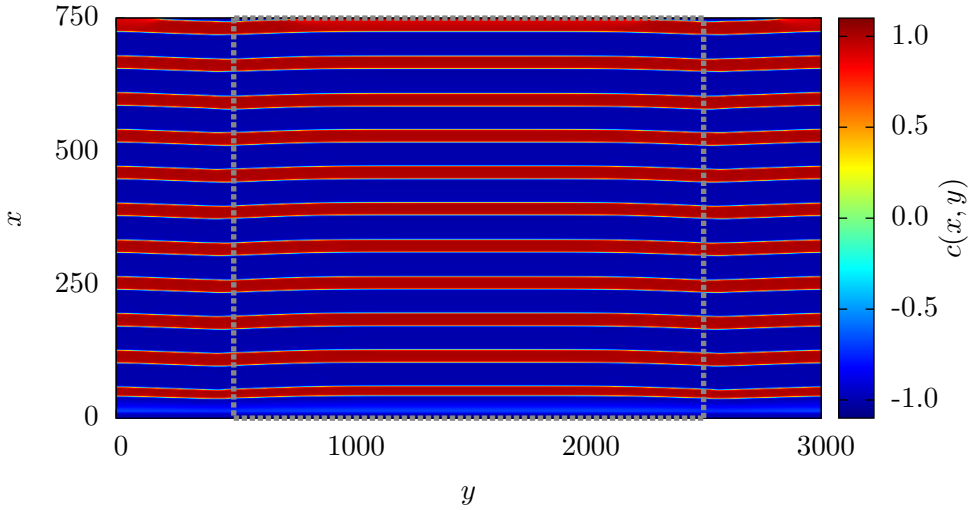

Figure 5.10: Snapshot of a two-dimensional simulation, where the transfer onto a prestructured substrate is simulated. The prestructure consists of stripes with $L_{\mathrm{pre}} = 400$ that reach from $y = 500$ to $y = 2500$ (depicted by the gray dashed lines). The solution exhibits bending of the occurring stripes at the boundary of the prestructure stripes.

6 Linear stability analysis

The results in the previous chapters were mainly achieved by direct numerical simulations of the model (2.22). Now we are looking for a different approach to investigate the system. In particular, we want to gain more insights in the transition from stationary solutions to time periodic solutions by means of linear stability analysis.

In general, a linear stability analysis is a tool to determine the stability of a solution of an equation with respect to a small perturbation. We again start with the model Eq. (2.22),

$$\begin{aligned}\frac{\partial}{\partial t}c(\mathbf{x},t) &= -\nabla\cdot\left[-\nabla\left(-\Delta c(\mathbf{x},t) - c(\mathbf{x},t) + c(\mathbf{x},t)^3 + \mu\zeta(x)\right) + \mathbf{v}c(\mathbf{x},t)\right] \\ &=: \mathscr{F}(\nabla,\mathbf{x},\mathbf{v})\left[c(\mathbf{x},t)\right], \end{aligned} \tag{6.1}$$

where we introduced $\mathscr{F}(\nabla,\mathbf{x},\mathbf{v})[\cdot]$ as a short-hand notation for the nonlinear operator defined by the right-hand side of the evolution equation. Now, the starting point is the assumption of the existence of a stationary solution $\tilde{c}(\mathbf{x})$, and we are interested in the temporal evolution of this solution under the influence of a small perturbation $\eta(\mathbf{x},t)$,

$$c(\mathbf{x},t) = \tilde{c}(\mathbf{x}) + \eta(\mathbf{x},t). \tag{6.2}$$

Inserting this ansatz into the model, we obtain

$$\frac{\partial}{\partial t}\tilde{c}(\mathbf{x}) + \frac{\partial}{\partial t}\eta(\mathbf{x},t) = \mathscr{F}(\nabla,\mathbf{x},\mathbf{v})\left[\tilde{c}(\mathbf{x}) + \eta(\mathbf{x},t)\right], \tag{6.3}$$

where we can expand the right-hand side into a Taylor series of $\mathscr{F}$ about $c(\mathbf{x},t) = \tilde{c}(\mathbf{x})$,

$$\begin{aligned}\frac{\partial}{\partial t}\tilde{c}(\mathbf{x}) + \frac{\partial}{\partial t}\eta(\mathbf{x},t) =& \mathscr{F}(\nabla,\mathbf{x},\mathbf{v})\left[\tilde{c}(\mathbf{x})\right] + \mathscr{F}'(\nabla,\mathbf{x},\mathbf{v})\big|_{\tilde{c}(\mathbf{x})}\,\eta(\mathbf{x},t) \\ &+ \frac{1}{2}\,\mathscr{F}''(\nabla,\mathbf{x},\mathbf{v})\big|_{\tilde{c}(\mathbf{x})}\,\eta(\mathbf{x},t) : \eta(\mathbf{x},t) + \mathcal{O}(\eta^3). \end{aligned} \tag{6.4}$$

Here, $\mathscr{F}'$ is a linear operator denoting the Fréchet-derivative of the nonlinear operator $\mathscr{F}$. For the case of Eq. (6.1), it takes the form

$$\mathscr{F}'(\nabla,\mathbf{x},\mathbf{v})\big|_{\tilde{c}(\mathbf{x})} = -\Delta^2 + \left(3\tilde{c}^2 - 1\right)\Delta + \left(12\tilde{c}\nabla\tilde{c} - \mathbf{v}\right)\cdot\nabla + 6\left(\tilde{c}\Delta\tilde{c} + (\nabla\tilde{c})^2\right). \tag{6.5}$$

The first terms on both sides of Eq. (6.4) vanish because $\tilde{c}(\mathbf{x})$ was assumed to be a solution of Eq. (6.1). If we additionally neglect the terms of higher order, we obtain a linear evolution equation for the perturbation $\eta(\mathbf{x},t)$,

$$\frac{\partial}{\partial t}\eta(\mathbf{x},t) = \mathscr{F}'(\nabla,\mathbf{x},\mathbf{v})\big|_{\tilde{c}(\mathbf{x})}\,\eta(\mathbf{x},t). \tag{6.6}$$

The perturbation can now be written as a series of eigenfunctions $\eta_\mathrm{j}(\mathbf{x})$ of $\mathscr{F}'$ with the assumption of an exponential time dependence with exponent λ_j,

$$\eta(\mathbf{x},t) = \sum_\mathrm{j} \eta_\mathrm{j}(\mathbf{x}) e^{\lambda_\mathrm{j} t}. \tag{6.7}$$

By inserting this ansatz into Eq. (6.6) and evaluating the time derivative, we are left with the linear eigenvalue problem

$$\lambda_\mathrm{j}\eta_\mathrm{j}(\mathbf{x}) = \mathscr{F}'(\nabla,\mathbf{x},\mathbf{v})\big|_{\tilde{c}(\mathbf{x})}\,\eta_\mathrm{j}(\mathbf{x}). \tag{6.8}$$

Statements about the linear stability of the solution $\tilde{c}(\mathbf{x})$ can now be made by looking at the eigenvalues λ_j. The Hartmann-Grobmann theorem now states that the solution $\tilde{c}(\mathbf{x})$ is stable if the real parts of all eigenvalues are less than zero, $\mathrm{Re}(\lambda_\mathrm{j}) < 0\ \forall\,\mathrm{j}$, or unstable if there is at least one eigenvalue with a positive real part, $\exists\ j:\ \mathrm{Re}(\lambda_\mathrm{j}) > 0$ [Str08]. If the largest real part of an eigenvalue is equal to zero, no statement on the stability of the solution can be made by means of a linear stability analysis.

Typically, one is now interested in the behavior of the stability when varying certain control parameters. In our case, the main control parameter is the transfer velocity $\mathbf{v}$ that on the one hand enters the linearization operator explicitly, but on the other hand also in addition implicitly via the stationary solution $\tilde{c}(\mathbf{x})$, which of course also differs for varying $\mathbf{v}$.

6.1 Application to the model

In contrast to typical textbook examples, in our case the linearization is not calculated about a homogeneous but a spatially inhomogeneous state $\tilde{c}(\mathbf{x})$. In particular, we want to investigate the stability of type 2 solution (see Fig. 4.2) close to the onset of pattern formation. Therefore, the linearized operator $\mathscr{F}'$ has a spatial dependence, too, and the eigenfunctions cannot be assumed to be well represented by a plane wave ansatz, as it is often used. To account for these facts, the approach used in the following starts with a stationary solution $\tilde{c}(\mathbf{x})$ obtained by direct numerical simulations. The solution is then inserted into Eq. (6.5) to evaluate $\mathscr{F}'(\nabla,\mathbf{x},\mathbf{v})|_{\tilde{c}(\mathbf{x})}$. The operators in (6.5) are discretized by means of finite difference schemes on the same grid as the numerical solution $\tilde{c}(\mathbf{x})$. The actual implementation is done in MATLAB.

We first consider the one-dimensional case, where the linearization operator (6.5) then reads

$$\begin{aligned}\mathscr{F}'(\nabla,x,v)\big|_{\tilde{c}(x)} = &-\frac{\partial^4}{\partial x^4} + \left(3\tilde{c}^2-1\right)\frac{\partial^2}{\partial x^2} + \left(12\tilde{c}\frac{\partial\tilde{c}}{\partial x} - v\right)\frac{\partial}{\partial x} \\ &+ 6\left(\tilde{c}\frac{\partial^2\tilde{c}}{\partial x^2} + \left(\frac{\partial\tilde{c}}{\partial x}\right)^2\right).\end{aligned} \tag{6.9}$$

After the discretization, the operator $\mathscr{F}'$ is represented by a matrix. The eigenvalues and eigenvectors of this matrix are then the eigenvalues and eigenfunctions of the eigenvalue problem (6.8). The results of this approach are shown in

Fig. 6.1, where a stationary solution of type 2 for $v = 0.0259$ (corresponding to the transfer of a homogeneous LC layer) and five eigenfunctions corresponding to the first five eigenvalues with the largest real part are shown. The transfer velocity is close to the instability threshold, where the patterning regime begins. Therefore, the eigenfunctions give a clue where exactly in terms of local position the instability occurs. All five eigenfunctions in Fig. 6.1 feature a dominant peak located at the position of the meniscus, where the solutions of type 2 exhibit a steep increase up to a value near $c = +1$. The eigenfunctions only differ in the area behind the meniscus, where $c(x)$ is nearly constant and the shape of the eigenfunctions reminds of basic harmonics. This shape of the eigenfunctions gives strong evidence that the formation of stripes occurs right at the meniscus and not due to an instability of the nearly homogeneous area behind the meniscus.

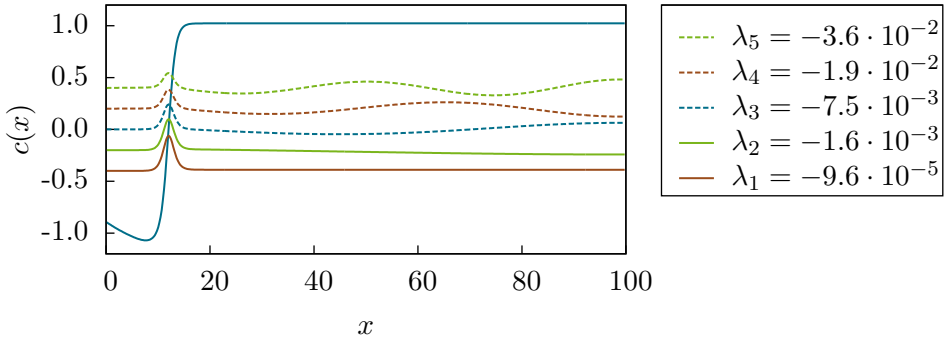

Figure 6.1: Stationary solution of type 2 (blue solid line) for $v = 0.0258$ and five eigenfunctions corresponding to the first five eigenvalues λ_1-λ_5 with the largest real part obtained by linear stability analysis. The eigenfunctions are shifted along the c-axis for better visibility. The real part of the corresponding eigenvalue decreases from bottom (red solid line) to top (green dashed line).

As mentioned above, statements on the stability of a certain solution can be made by looking at the eigenvalue with the largest real part (from now on only referred to as largest eigenvalue). To this end, we come back to Fig. 4.6, where the results from direct numerical simulations were shown in an L^2 versus v diagram. Figure 6.2 adopts this representation and additionally shows the corresponding real part of the largest eigenvalue. The fact that the real parts are less than zero for the bulk of the branches clearly proves the stability of these stationary solutions. Up to now, we only stated the stability of the solutions because of numerical observations. However, direct numerical simulations can never really prove the stability because one can never distinguish a very slow transient behavior from a stable stationary solution by means of simulations of finite times. The increase of the real parts of the eigenvalues above zero at the edges of the branches indicate that the branches really end at the locations observed by the simulations because they become unstable.

In this context, we again want to point to results from the literature concerning the same model. In [KGFT12], the nature of the bifurcation leading

to the onset of the patterning regime was investigated. It has turned out that the patterning branch in Fig. 6.2 (blue solid line) does not arise from the end of the branch of the solution type 2 (red solid line), but from a branch that is unstable. Therefore, there exists a global bifurcation that cannot be tracked down to a single solution, where a single eigenfunction becomes unstable. In contrast, a whole region in the solution space has to be considered, which of course is not possible by means of linear stability analysis of a local solution. For the analysis in this section, this implies that the transition from the stable solutions of type 2 to the periodic solutions cannot be simply envisioned by a single consequently growing perturbation leading to the onset of pattern formation. The statements made on the stability of the solutions of course remain unchanged by the nature of the bifurcation.

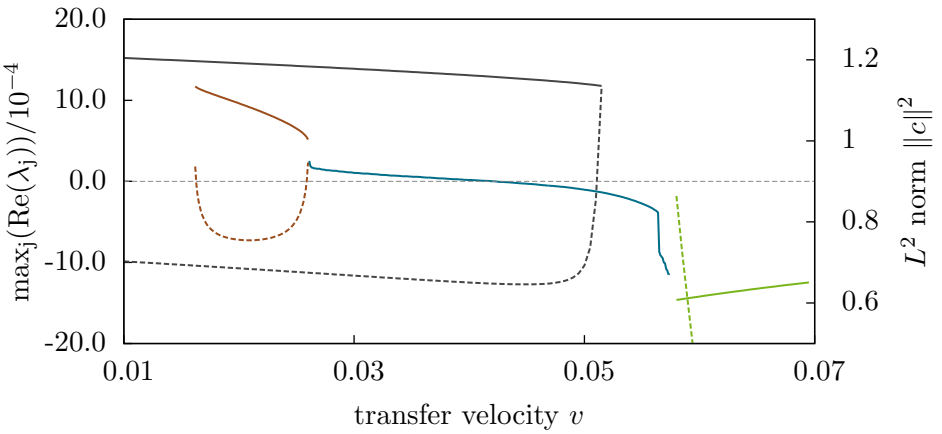

Figure 6.2: Branches of solutions (solid lines) and their corresponding eigenvalue with the largest real part (dashed lines). For the time-periodic solutions (blue line), no single eigenvalue can be assigned by means of a linear stability analysis.

6.2 Stability analysis in 2D

We now want to extend the technique presented in the previous section to the two-dimensional case. Especially, we are interested in the transition between stripes parallel to the meniscus to stripes perpendicular to the meniscus. Therefore, the ansatz for the perturbation is multiplied with a plane wave term in y-direction,

$$\eta(\mathbf{x}, t) = \sum_{\mathrm{j}} \eta_{\mathrm{j}}(x) e^{ik_y y} e^{\lambda_{\mathrm{j}} t}. \tag{6.10}$$

This ansatz is reasonable because we impose periodic boundary conditions in y-direction. The linearization operator then reads

$$\mathscr{F}'(\nabla, x, v)\big|_{\tilde{c}(x)} = -\frac{\partial^4}{\partial x^4} + 2k_y\frac{\partial^2}{\partial x^2} - k_y^4 + \left(3\tilde{c}^2 - 1\right)\frac{\partial^2}{\partial x^2} + k_y^2\left(3\tilde{c}^2 - 1\right) + \left(12\tilde{c}\frac{\partial\tilde{c}}{\partial x} - v\right)\frac{\partial}{\partial x} + 6\left(\tilde{c}\frac{\partial^2\tilde{c}}{\partial x^2} + \left(\frac{\partial\tilde{c}}{\partial x}\right)^2\right). \tag{6.11}$$

That is, for a fixed value of k_y, the same approach as in the one-dimensional case can then be applied. To reveal the dependence of the eigenvalue spectrum on the transversal wavenumber k_y, of course the approach has to be repeated for different values of k_y. Again, the solutions we want to analyze are obtained by one-dimensional direct numerical simulations, meaning we are interested in the stability of two-dimensional solutions that are homogeneous in y-direction.

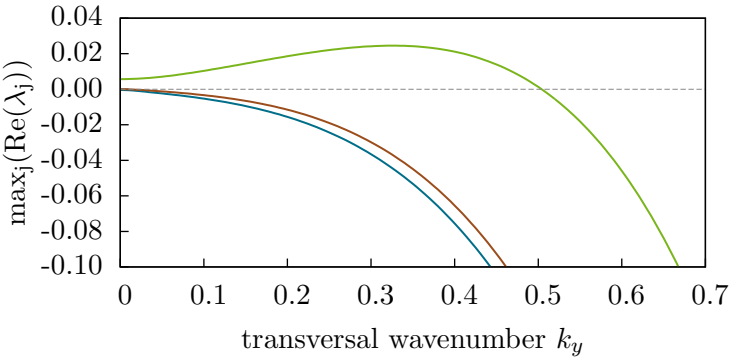

Figure 6.3: Real part of the eigenvalue with the largest real part $\max_j(\mathrm{Re}(\lambda_j))$ under the assumption of a transversal modulation of the perturbation with $e^{ik_y y}$. The different colors refer to different solutions for a transfer velocity $v = 0.0254$ (blue line), $v = 0.0260$ (red line), and $v = 0.0266$ (green line). The latter refers to a snapshot of a time-periodic solution.

The results, again for stationary solutions close to the onset of the patterning regime, are shown in Fig. 6.3. In the case of transfer velocities of $v = 0.0254$ and $v = 0.0260$, the real parts of the eigenvalues monotonically decrease with increasing k_y. This implies that stable stationary solutions that are homogeneous in y-direction are also stable with respect to perturbations that vary with y. This is an important result because it attests that the results from the one-dimensional linear stability analysis performed in the previous section fully carry over to the two-dimensional case. In addition, we can take a look at the results for time-periodic solutions. For an increased transfer velocity of $v = 0.0266$ above the lower limit of the patterning regime, the dependence of the eigenvalues of k_y changes qualitatively. Then the real part of the largest eigenvalue increases with the transversal wavenumber k_y up to a maximum value, and then decreases. That is, if we consider a solution that is already unstable, the solution is even more sensitive to perturbations that have a certain variation in y-direction. These results reveal that the transversal instability in the two-

dimensional system is indeed a secondary instability because it only appears in the wake of the first instability that also occurs in the one-dimensional system and that is homogeneous in the y-direction. This also explains the way the stripes perpendicular to the meniscus evolve in the numerical simulations (see, e.g., Fig. 4.13): First, stripes parallel to the meniscus are formed, which then subsequently break up in y-direction and extend in x-direction, until stripes perpendicular to the meniscus are formed. Of course, it has to be emphasized that the eigenvalue spectrum obtained by this approach varies in time for a periodic solution, like the one studied for $v = 0.0266$ in Fig. 6.3, and therefore rigorous statements for such solutions would necessitate a different approach, like the Floquet theory [AFHF10]. Nevertheless, we can find evidence that the

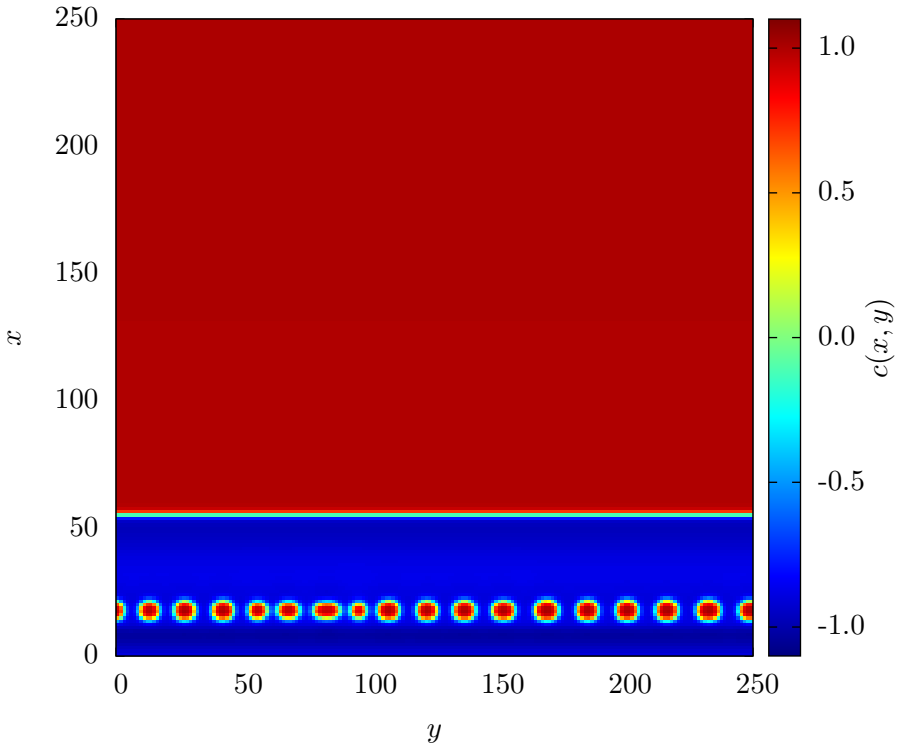

Figure 6.4: Snapshot of 2D simulation showing a very early stage of the formation of transversal stripes.

approach used here is able to deliver reasonable results. To this end, we take a look at a two-dimensional simulation in an early stage before the occurrence of stripes perpendicular to the meniscus. The initial conditions for the simulation shown in Fig. 6.4 were perturbed by white noise, so that the system was able to "choose" a preferred wavelength. By the basic approach of counting the number of max ima n_{maxima} that arise located at the meniscus, we can easily

estimate the average wavenumber of the structure to be

$$k_y = \frac{2\pi}{\lambda_y} = \frac{2\pi}{\frac{L_y}{n_{\text{maxima}}}} \approx 0.43. \tag{6.12}$$

Taking into account the simplicity of this estimation, the value obtained resembles the wavenumber with the largest amplification predicted by the stability analysis in Fig. 6.3, $k_y = 0.325$, quite well, especially when comparing the corresponding eigenvalues that differ only slightly (see Fig. 6.3). The fact that the results do not coincide perfectly, however, is not surprising as the linear stability analysis does only deliver predictions for infinitesimal perturbations, while the perturbation observable in Fig. 6.4 has obviously evolved much further already.

The mechanism that leads to the fact that for higher transfer velocities stripes parallel to the meniscus stay stable and do not break up unfortunately cannot be addressed with the linear stability analysis presented here. Instead, a mathematical technique like the already mentioned Floquet theory, which is able to treat time-periodic solutions correctly, is planned to be employed in future work to investigate the solutions inside the patterning regime. Still, the linear stability analysis presented in this chapter already reveals insights in the transfer process. It proves the stability of the stationary solutions obtained by direct numerical simulations, it discloses the functional form of eigenfunctions involved in the onset of pattern formation, and it reveals that stripes perpendicular to the meniscus can only occur in the wake of a first instability leading to stripes parallel to the meniscus.

7 Summary and Outlook

The main topic of this thesis is the investigation of pattern formation processes in Langmuir-Blodgett transfer by means of a minimal Cahn-Hilliard model. To this end, first a derivation of a Cahn-Hilliard model is presented that is suitable for the application to the case of Langmuir-Blodgett transfer and that has been first derived in [KGFT12] and in more details in [Köp11]. The resulting model (2.22) used in this thesis incorporates physical effects occurring during Langmuir-Blodgett transfer, like substrate-mediated condensation, energetic boundary layer contributions, advection, as well as certain boundary conditions, into the framework of a Cahn-Hilliard equation. These are the key ingredients making this Cahn-Hilliard model suitable for the investigation of pattern formation processes during Langmuir-Blodgett transfer. To this end, direct numerical simulations of the model have been performed. The simulation software was programmed in the programming language C++ using the CUDA framework for computations on modern graphics processors. The software employs a finite difference approach for the evaluation of spatial derivatives on the simulation grid and an adaptive Runge-Kutta time stepping algorithm. The first investigations with this approach have been done on the case of a transfer onto a homogeneous substrate in one and two dimensions, where some results are readily available in the literature [KGFT12]. These results, like the transfer velocity dependence of the wavelength of the occurring stripe patterns, or the transition between stripes of different orientation, can be compared to the results obtained here and therefore be used as a benchmark for the actual implementation. With the confidence of a properly working model and numerical implementation, new dynamical scenarios have been investigated. In particular, the results for periodic solutions in one dimension for a varying boundary concentration c_0 (see Figs. 4.9-4.10) reveal that this parameter can be used experimentally to control certain properties of the transferred patterns. Two-dimensional simulations for varying c_0 are also worth to be investigated in future work.

In the same context, we have also identified a minor drawback of the model. At the upper limit of the patterning regime, the spatial location where new stripes are formed is carried further and further away from the meniscus with an increasing transfer velocity. The patterning process then ceases, as soon as this location is carried outside the simulation domain. As the results indicate, this effect becomes larger for an increasing value of c_0 (see the irregular behavior of $k(v, c_0)$ at the right limit of the patterning regime in Fig. 4.9). This result implies a dependence of the upper limit of the patterning regime on the size of the simulation domain, which of course is an unwanted artifact in the simulation. It occurs because we assumed the mobility M of the monolayer to be constant in the derivation of the model. A more realistic approach could

be achieved in future investigations by using an ansatz for M that restricts the mobility to a certain domain around the meniscus, just as in the real experiment, where the monolayer also is "frozen" as soon as the liquid layer below it is evaporated.

In addition to the conventional Langmuir-Blodgett transfer onto homogeneous substrates, also Langmuir-Blodgett rotating transfer has been examined in chapter 4. The results from simulations resemble the experimental observation that this novel approach can be used to produce gradient structures as well as to do high-throughput studies, where a full parameter range can be evaluated by just one transfer experiment. This example demonstrates the ability of the model to be applied to different transfer geometries.

The results presented in chapter 5 attend to the transfer onto substrates with a prestructure. Here it has been proven that prestructures are a powerful way to control the pattern formation process during Langmuir-Blodgett transfer. While this has been shown in the framework of the full model earlier [KGF11], the findings of this thesis show for the first time that such effects can be also be studied in the minimal Cahn-Hilliard model. Therefore, a reasonable subject for future research is the application of the model onto the case of more complex prestructures. Although we have been able to address a key feature of experimental findings in this context, that is, the bending of occurring stripes at the boundaries of a prestructure, there are still open questions concerning the mechanisms involved. One major question is the validity of the assumption of a static meniscus when considering prestructured substrates that do not only exhibit a chemical prestructure influencing the substrate-mediated condensation, but possibly also a topological prestructure influencing the dynamics of the meniscus. This should be investigated by comparative simulations of both the full model and the minimal Cahn-Hilliard model.

In the last chapter, the technique of linear stability analysis has been utilized to examine the stability of the solutions obtained by direct numerical solutions. Further, the occurrence of stripes perpendicular to the meniscus has been identified to arise as a transversal (secondary) instability only in the wake of the global bifurcation leading to stripes parallel to the meniscus. An open question that should be addressed in future work concerns the stability of stripes parallel to the meniscus for higher velocities, where this secondary instability does not occur. To face this fact, a technique has to be employed that is capable of treating not only stationary solutions, but is also able to make statements on the stability of time-periodic solutions. The Floquet theory seems to be a reasonable choice for such investigations. With such a technique, it should also be possible to examine the experimental observation of rectangular patterns, which probably can be explained as a superposition of stripes perpendicular and parallel to the meniscus.

Looking at the results obtained in this thesis, the Cahn-Hilliard model has proven to be a powerful framework to investigate the pattern formation phenomena occurring during Langmuir-Blodgett transfer. While being much less complex than the full model that was first developed to investigate the same phenomena, the minimal Cahn-Hilliard model reproduces the main features obtained in the full model.

Bibliography

[AFHF10] J. Argyris, G. Faust, M. Haase, and R. Friedrich. *Die Erforschung des Chaos: Eine Einführung in die Theorie nichtlinearer Systeme.* Springer Complexity. Springer, 2010.

[Blo34] K.B. Blodgett. Monomolecular films of fatty acids on glass. *Journal of the American Chemical Society*, 56(2):495, 1934.

[Blo35] K.B. Blodgett. Films built by depositing successive monomolecular layers on a solid surface. *Journal of the American Chemical Society*, 57(6):1007–1022, 1935.

[But08] J.C. Butcher. *Numerical Methods for Ordinary Differential Equations.* John Wiley & Sons, 2008.

[CFL28] R. Courant, K. Friedrichs, and H. Lewy. Über die partiellen Differenzengleichungen der mathematischen Physik. *Mathematische Annalen*, 100(1):32–74, 1928.

[CH58] J.W. Cahn and J.E. Hilliard. Free energy of a nonuniform system. I. Interfacial free energy. *The Journal of Chemical Physics*, 28:258, 1958.

[CH93] M.C. Cross and P.C. Hohenberg. Pattern formation outside of equilibrium. *Reviews of Modern Physics*, 65(3):851, 1993.

[CHFC07] X. Chen, M. Hirtz, H. Fuchs, and L. Chi. Fabrication of Gradient Mesostructures by Langmuir-Blodgett Rotating Transfer. *Langmuir*, 23(5):2280–2283, 2007.

[CLH+07] X. Chen, S. Lenhert, M. Hirtz, N. Lu, H. Fuchs, and L. Chi. Langmuir–Blodgett Patterning: A Bottom–Up Way To Build Mesostructures over Large Areas. *Accounts of Chemical Research*, 40(6):393–401, 2007.

[Dem03] W. Demtröder. *Experimentalphysik 1.* Springer, 3. edition, 2003.

[GHLL99] H. Gau, S. Herminghaus, P. Lenz, and R. Lipowsky. Liquid morphologies on structured surfaces: from microchannels to microchips. *Science*, 283(5398):46–49, 1999.

[GK97] A.Y. Grosberg and A.R. Khokhlov. *Giant molecules.* World Scientific, 1997.

[HL10] J. Hao and Y. Li. Self-organized DPPC patterns on prestructured substrates. Unpublished Talk, 2010.

[KGF09] M.H. Köpf, S.V. Gurevich, and R. Friedrich. Thin film dynamics with surfactant phase transition. *EPL (Europhysics Letters)*, 86(6):66003, 2009.

[KGF11] M.H. Köpf, S.V. Gurevich, and R. Friedrich. Controlled nanochannel lattice formation utilizing prepatterned substrates. *Physical Review E*, 83(1):016212, 2011.

[KGFC10] M.H. Köpf, S.V. Gurevich, R. Friedrich, and L. Chi. Pattern formation in monolayer transfer systems with substrate-mediated condensation. *Langmuir*, 26(13):10444–10447, 2010.

[KGFT12] M.H. Köpf, S.V. Gurevich, R. Friedrich, and U. Thiele. Substrate-mediated pattern formation in monolayer transfer: a reduced model. *New Journal of Physics*, 14(2):023016, 2012.

[Köp11] M.H. Köpf. *On the dynamics of surfactant covered thin liquid films and the formation of stripe patterns in Langmuir-Blodgett transfer*. PhD thesis, Westfälische Wilhelms-Universität Münster, 2011.

[Lan34] I. Langmuir. Mechanical properties of monomolecular films. *Journal of the Franklin Institute*, 218(2):143–171, 1934.

[LLM88] M.J. Litzkow, M. Livny, and M.W. Mutka. Condor - A Hunter of Idle Workstations. In *8th International Conference on Distributed Computing Systems*, pages 104–111. IEEE, 1988.

[MKS+12] J. Moghal, J. Kobler, J. Sauer, J. Best, M. Gardener, A.A.R. Watt, and G. Wakefield. High-Performance, Single-Layer Antireflective Optical Coatings Comprising Mesoporous Silica Nanoparticles. *ACS Applied Materials & Interfaces*, 4(2):854–859, 2012.

[NCS84] A. Novick-Cohen and L.A. Segel. Nonlinear aspects of the Cahn-Hilliard equation. *Physica D: Nonlinear Phenomena*, 10(3):277–298, 1984.

[Nol12] W. Nolting. *Grundkurs Theoretische Physik 4: Spezielle Relativitätstheorie, Thermodynamik*. Springer-Lehrbuch. Springer, 2012.

[NVI] NVIDIA. CUDA C Programming Guide Version 4.2. `http://docs.nvidia.com/cuda/cuda-c-programming-guide/index.html`. last visited on November 7th, 2012.

[ODB97] A. Oron, S.H. Davis, and S.G. Bankoff. Long-scale evolution of thin liquid films. *Reviews of Modern Physics*, 69(3):931, 1997.

[Poc91] A. Pockels. Surface tension. *Nature*, 43(1115):437–439, 1891.

[Poc93] A. Pockels. Relations between the surface-tension and relative contamination of water surfaces. *Nature*, 48:152–154, 1893.

[PRK03] A. Pikovsky, M. Rosenblum, and J. Kurths. *Synchronization: A Universal Concept in Nonlinear Sciences*. Cambridge Nonlinear Science Series. Cambridge University Press, 2003.

[PTVF92] W.H. Press, S.A. Teukolsky, W.T. Vetterling, and B.P. Flannery. *Numerical Recipes in C: The Art of Scientific Computing*. Cambridge University Press, 2. edition, 1992.

[QXX+99] D. Qin, Y. Xia, B. Xu, H. Yang, C. Zhu, and G.M. Whitesides. Fabrication of Ordered Two-Dimensional Arrays of Micro- and Nanoparticles Using Patterned Self-Assembled Monolayers as Templates. *Advanced Materials*, 11(17):1433–1437, 1999.

[Rec06] P. Rechenberg. *Informatik-Handbuch*. Hanser, 2006.

[RL07] R.K. Roy and K.R. Lee. Biomedical applications of diamond-like carbon coatings: A review. *Journal of Biomedical Materials Research Part B: Applied Biomaterials*, 83(1):72–84, 2007.

[Rob90] G. Roberts, editor. *Langmuir-Blodgett Films*. Plenum Press New York, 1990.

[RS92] H. Riegler and K. Spratte. Structural changes in lipid monolayers during the langmuir-blodgett transfer due to substrate/monolayer interactions. *Thin Solid Films*, 210:9–12, 1992.

[SGS10] J.E. Stone, D. Gohara, and G. Shi. OpenCL: A parallel programming standard for heterogeneous computing systems. *Computing in science & engineering*, 12(3):66, 2010.

[Smi86] G.D. Smith. *Numerical Solution of Partial Differential Equations: Finite Difference Methods*. Oxford Applied Mathematics And Computing Science Series. Oxford University Press, USA, 1986.

[Str08] S.H. Strogatz. *Nonlinear Dynamics And Chaos*. Studies in Nonlinearity. Westview Press, 2008.

Danksagung

Während der Entstehung dieser Arbeit, aber auch schon in den Jahren des Studiums zuvor, waren viele Menschen durch Ihre Unterstützung maßgeblich am Erfolg dieser Arbeit und meines Studiums beteiligt. Daher möchte ich an dieser Stelle meinen Dank aussprechen:

- Herrn Professor Dr. Rudolf Friedrich für die Möglichkeit, dieses Thema bearbeiten zu können, seine Betreuung, die vielen hilfreichen Diskussionen und die Vermittlung seiner Begeisterung für das Thema. Leider konnte er das Ende dieser Arbeit nicht mehr erleben.
- Frau Dr. Svetlana Gurevich für die Übernahme der Betreuung und Begutachtung dieser Arbeit, ihre immer offen stehende Tür, die fachlichen Ratschläge und nicht zuletzt auch das Korrekturlesen dieser Arbeit.
- Prof. Dr. Andreas Heuer für die schnelle und unkomplizierte Bereitschaft ebenfalls als Gutachter für diese Arbeit zur Verfügung zu stehen.
- Meinem Bruder Dr. Michael Wilczek für die fortwährende private und fachliche Unterstützung während meines gesamten Studiums und auch für das Korrekturlesen dieser Arbeit.
- Meinen Bürokollegen Eva Baresel, Anton Daitche und Iñigo Montero für die wunderbare Atmosphäre in unserem Büro.
- Allen weiteren Mitgliedern der Arbeitsgruppe Friedrich für nette Mittags- und Kaffeepausen, interessante AG-Seminare und eine angenehme Zeit.
- Meinen Korrekturlesern Anton Daitche, Christoph Honisch und Walter Tewes für den Kampf gegen Fehler und schlechten Stil.
- Meiner Familie für die bedingungslose Unterstützung seitdem ich denken kann.
- Christina Wohlers für Ihre Liebe und die ständige Unterstützung tagein und tagaus.

Erklärung zur Masterarbeit

Hiermit versichere ich, die vorliegende Masterarbeit selbstständig angefertigt und außer den angegebenen keine weiteren Hilfsmittel verwendet zu haben.

Münster, den 12. Dezember 2012